THESIS FOR THE DEGREE OF LICENTIATE OF PHILOSOPHY

Acceptor-doped barium zirconate: Oxidation, hydration and space-charge formation

ANDERS LINDMAN

Department of Applied Physics
CHALMERS UNIVERSITY OF TECHNOLOGY
Göteborg, Sweden 2015

Acceptor-doped barium zirconate: Oxidation, hydration and space-charge formation
ANDERS LINDMAN

Department of Applied Physics
Chalmers University of Technology
SE-412 96 Göteborg, Sweden
Telephone +46 31 772 10 00

Cover: The relaxed structure and localized charge density of a +2 charged oxygen vacancy in $BaZrO_3$.

Typeset in XeLaTeXwith Times Ten and Akzidenz-Grotesk. Figures created using ASE, Vesta, XcrySDen and matplotlib.

Chalmers reproservice
Göteborg, Sweden 2015

Acceptor-doped barium zirconate: Oxidation, hydration and space-charge formation

ANDERS LINDMAN
Department of Applied Physics
Chalmers University of Technology

Abstract

The current production and use of fossil fuels is not sustainable and new technologies are needed to become more independent of these fuels. The hydrogen economy, with the fuel cell as an efficient converter of chemical to electrical energy, is a desirable alternative. For this to become a reality, new materials with tailored properties are required. The effort to find suitable materials could be helped if the different mechanisms that govern the desired properties are well understood.

The work done in this thesis has been an effort to address two problems concerning the ionic and electronic conductivity in perovskite oxides, which is a class of materials suitable for the use in solid oxide fuel cells (SOFCs) and related technologies. The research is theoretical and combines atomistic simulations and thermodynamic modeling.

The first study is more general and deals with how accurately electronic structure-based methods can treat oxidation and hydration of these materials. Acceptor-doped $BaZrO_3$ is chosen as a model system. Three methods have been considered: Density functional theory with PBE (a GGA functional) and PBE0 (a hybrid functional), and the G_0W_0 method. While the hydration reaction is well described by all methods the oxidation reaction is found to differ in a qualitative manner. The reaction is found to be exothermic with PBE and endothermic by the two others. The latter scenario is more consistent with experimental data on reaction enthalpies, carrier concentrations and electrical conductivities.

The second problem is more specific and concerns the proton conductivity in acceptor-doped $BaZrO_3$, which has great potential as electrolyte material in proton-conducting SOFCs due to the combination of high chemical stability and high bulk proton conductivity. The problem lies in the grain boundaries, which have a deteriorating effect on the total proton conductivity due to the presence of space-charges at these interfaces. The mechanism behind space-charge formation is found to be segregation of charged oxygen vacancies and protons to the grain boundaries, where protons give the largest contribution under fuel cell operating conditions.

Keywords: perovskites, $BaZrO_3$, oxidation, hydration, space charge, point defects, grain boundaries, density functional theory, *GW*, interatomic potentials.

LIST OF PUBLICATIONS

This thesis consists of an introductory text and the following papers:

I **Implications of the band gap problem on oxidation and hydration in acceptor-doped barium zirconate**
Anders Lindman, Paul Erhart and Göran Wahnström
(In preparation)

II **Oxygen vacancy segregation in grain boundaries of $BaZrO_3$ using interatomic potentials**
Anders Lindman, Edit E. Helgee, B. Joakim Nyman and Göran Wahnström
Solid State Ionics **230**, 27-31 (2013)

III **Origin of space charge in grain boundaries of proton-conducting $BaZrO_3$**
Edit E. Helgee, Anders Lindman and Göran Wahnström
Fuel Cells **13**, 19-28 (2013)

IV **Theoretical modeling of defect segregation and space-charge formation in the $BaZrO_3$ (210)[001] tilt grain boundary**
Anders Lindman, Edit E. Helgee and Göran Wahnström
Solid State Ionics **252**, 121-125 (2013)

The author's contributions to the papers:

I The author did the DFT calculations and the modeling and wrote the paper.

II The author did most of the calculations and the modeling and was the main author of the paper.

III The author did part of the calculations and the modeling and assisted in writing the paper.

IV The author did the calculations and the modeling and wrote the paper.

Contents

1

Introduction

Today, the global society relies on the use and production of fossil fuels. This has a negative impact on the environment in terms of pollution as well as global warming due to emission of greenhouse gases. There are also economical and political aspects to this as most of the world's deposits of oil are limited to quite a few areas, many which lie in unstable regions. On top of this, much of the fossil fuels have already been extracted and the supply will be limited in a not too distant future. Thus, sustainable alternatives are essential to meet energy demands in the future.

While there are sustainable commercial options already on the market such as solar cells and wind power, a completely new energy infrastructure will be required in the future in order to become completely independent of fossil fuels. One of the most promising alternatives is the *hydrogen economy* [1], where hydrogen serves as energy carrier. The chemical energy stored in hydrogen can be released through the reaction with oxygen, where water is the only byproduct in the ideal situation:

$$H_2 + \frac{1}{2}O_2 \longrightarrow H_2O \tag{1.1}$$

The hydrogen economy can be divided into three main parts: *production*, *storage* and *use*. All these stages have to be optimized in order for hydrogen to be a viable energy source, and at moment none of them have reached the necessary requirements. Hydrogen can be produced by the splitting of water in electrolyzer cells, which ideally are driven by solar power. The storage of hydrogen is a delicate problem where volume and weight restrictions pose the largest difficulty, especially for mobile applications. The last stage, which is to extract the energy for use, is where the fuel cell comes into play. The fuel cell convert the chemical energy stored in hydrogen to electrical energy and is much more efficient compared to combustion and heat engines.

While the work in this thesis in principle can be applied to a wide range of applications within the hydrogen economy, the focus of this introduction will be the fuel cell. More precisely, the solid oxide fuel (SOFC) cell will be considered, and this is the topic of the next section. For more comprehensive reviews on the subject of fuel cell systems see e.g., [2–4].

1.1 Solid oxide fuel cells

A solid oxide fuel cell (SOFC) constitutes of three main parts: the *anode*, the *electrolyte* and the *cathode*. A schematic representation of both oxide ion and proton conducting SOFCs is shown in Fig. 1.1. The reaction in Eq. 1.1 takes place in several steps at these different parts. The fuel enters at the anode where the hydrogen is oxidized to form protons and electrons according to

$$\mathrm{H_2} \longrightarrow 2\mathrm{H^+} + 2\mathrm{e^-} \tag{1.2}$$

On the other side of the cell at the cathode, oxygen is reduced according to

$$\frac{1}{2}\mathrm{O_2} + 2\mathrm{e^-} \longrightarrow \mathrm{O^{2-}} \tag{1.3}$$

Ions then diffuse through the electrolyte while the electronic charge carriers travel through an external load and generate electricity. Finally, the protons and the oxide ions form water through the reaction

$$2\mathrm{H^+} + \mathrm{O^{2-}} \longrightarrow \mathrm{H_2O} \tag{1.4}$$

The last reaction takes place either at anode if the electrolyte is an oxide ion conductor or at the cathode if it is a proton conductor. The latter scenario is more preferable since the water becomes separated from the fuel.

There are benefits and drawbacks with all fuel cells systems, and the SOFC is no different. The main benefits are that it contains only solid parts, there is no need for expensive catalysts and that hydrocarbons can also be used as fuel beside pure hydrogen. The main drawback are the high operating temperatures which require long start-up and shut-down times as well as it puts the materials under substantial thermal and chemical stress. While oxide ion conducting SOFCs are more established, proton-conducting SOFCs have gained much attention in recent years since they can operate at much lower temperatures [6].

Since the components of the fuel cell have different tasks, certain requirements are put on the conductive properties of the materials. The electrolyte needs to be an ionic conductor and an electronic insulator. The most commonly used materials for oxide ion conducting electrolytes are yttria-stabilized zirconia (YSZ) and

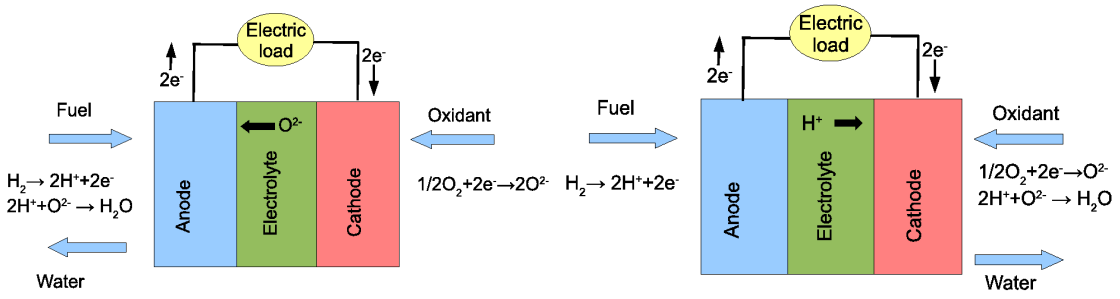

Figure 1.1: The working principle of an (a) oxide ion conducting and a (b) proton-conducting solid oxide fuel cell. Figures from [5].

gadolinium-doped ceria (GDC) which both crystallize in the fluorite structure, as well as strontium, magnesium-doped $LaGaO_3$ which is a perovskite [7, 8]. YSZ is most widely used but requires high operating temperatures (800-1000 °C). GDC on the other hand exhibit high conductivity at lower temperatures but then also becomes electronically conducting [8].

Acceptor-doped perovskites are popular materials for proton conducting electrolytes, which become proton conducting in wet atmospheres due to the hydration of oxygen vacancies. Since Iwahara *et. al.* [9] first discovered proton conduction in this class of materials back in 1981 many different compounds have been studied [8, 10, 11]. The most prominent perovskite proton conductors are $BaCeO_3$ and $BaZrO_3$, however they do come with some detrimental properties. The former is not stable with respect to CO and CO_2 while the latter is associated with a high grain boundary resistance and is difficult to sinter. Addressing the grain boundary-related problems of $BaZrO_3$ is one of the two main goals of this thesis.

There is large set of constraints put on the anode and cathode materials. First, they should be mixed conductors, exhibiting both high ionic and electronic conductivity. They should also have a high catalytic activity so that the oxidation and reduction reactions in Eq. 1.2 and Eq. 1.3 occur sufficiently fast and often. Furthermore, there is a huge difference between room temperature and operating temperatures, thus the thermal expansion becomes large. For the fuel cell to function properly it is important that the thermal expansion of the anode and cathode match that of the electrolyte. The appropriate choice of anode and cathode material is therefore to large extent determined by the electrolyte [7]. Many of the common anode and cathode materials have perovskite and fluorite structures. For specific examples see e.g., [6, 7, 12–14].

The electricity required to power most loads cannot be delivered by a single fuel cell. In practice, many cells are coupled in parallel to obtain the desired power. The component that connects the fuel cells is called an *interconnect*. The interconnects serve several purposes such as supporting each cell with fuel and transfer electricity from the cell, and, like for the electrodes, interconnect materials need to display a wide range of properties. These include high electronic conductivity, stability towards both oxidizing and reducing conditions (since the interconnect is in contact with both anodes and cathodes) as well as matching thermal expansion coefficients. The most suitable interconnect materials are based on chromium and a top contender is $LaCrO_3$ [15].

Beside the material properties mentioned here, other aspects need to be considered in order to obtain a commercially viable product. The fabrication process for a fuel cell must be relatively cheap and suitable for large-scale production. Furthermore, the abundance of certain elements is very low which puts further restriction on materials contain these elements [16].

To conclude, this section shows that designing a fuel cell is a difficult task, which requires tailor-made materials with fine-tuned properties. In order to succeed in this endeavor the underlying mechanisms for different properties need to be fully understood, and this is where theory and modeling becomes an important tool.

1.2 Thesis aim and outline

This thesis addresses two problems related to acceptor-doped perovskites when used as electrical conductors.

The first is one concerns the theoretical description of the oxidation of these materials. This reaction plays an important part in determining the conductive nature of these materials. The oxidation reaction is not well described by standard electronic structure methods since these fail to predict an accurate band gap. Methods beyond the standard approach have been applied to study the oxidation in $BaZrO_3$, which acts as a model system in this case. The aim here is to study to which extent the description of band gap affects the nature of this reaction.

The second problem is more directly related to acceptor-doped $BaZrO_3$. The total proton conductivity of these materials is severely limited by a low grain boundary conductivity, which is caused by space-charges at these boundaries. The aim here is to find the mechanism behind the space-charge formation by the means of atomistic and thermodynamic modeling.

The outline of this thesis is the following. Chapter 2 gives a background to the structure and properties of $BaZrO_3$ and perovskites in general. The following two chapters give a theoretical background to defect chemistry, space-charge formation and conductivity. Details regarding the computational methods used in this

work are given in Chapter 5. At last, Chapters 6 and 7 give a summary of the results and an outlook for future work.

2

Barium zirconate – a perovskite

The perovskite oxide family of materials has been of large interest for scientists over the last century since this class of materials exhibits a wide range of physical properties even though the crystal structure is quite simple. These materials have been shown to display properties such as piezoelectricity, pyroelectricity and ferroelectricity [17, 18], proton, ionic and electronic conductivity [11, 19, 20], superconductivity [21–23], ferromagnetism [24] and magnetoresistance [25, 26] with applications including but not limited to electrolytes and electrodes in fuel cells and electrolyzers [27, 28], non-volatile memories [29] and catalysts [30]. Perovskite oxides are ionic compounds with the general chemical formula ABO_3, where A and B are cations and O are oxygen anions. In the simplest structures is the A- and B-site only occupied by one cationic species each but there are more complex structures where more than one species are presented at each site.

Barium zirconate ($BaZrO_3$) is the material under main investigation in this thesis. This perovskite has been studied extensively since it in principle can combine high proton conductivity with chemical stability towards CO and CO_2 [6, 10]. With these properties it becomes a potential candidate as an electrolyte material for proton conducting fuels cells and electrolyzers. However, in practice the proton conductivity is often much lower. As will be clear further on, this is related to the *microstructure* of the material.

A crystalline material is to a large extent described by its lattice structure, i.e. the periodic arrangement of atoms within the material. In principle, this periodic arrangement can extend throughout the whole material, giving rise to a single crystal, but in practice this is most often not the case. Many solid materials are polycrystalline with a microstructure constituting of grains, where each grain is a single crystal. At the interface between two neighboring grains there is a mismatch in the periodic crystal structure, giving rise to a planar defect across the interface, which

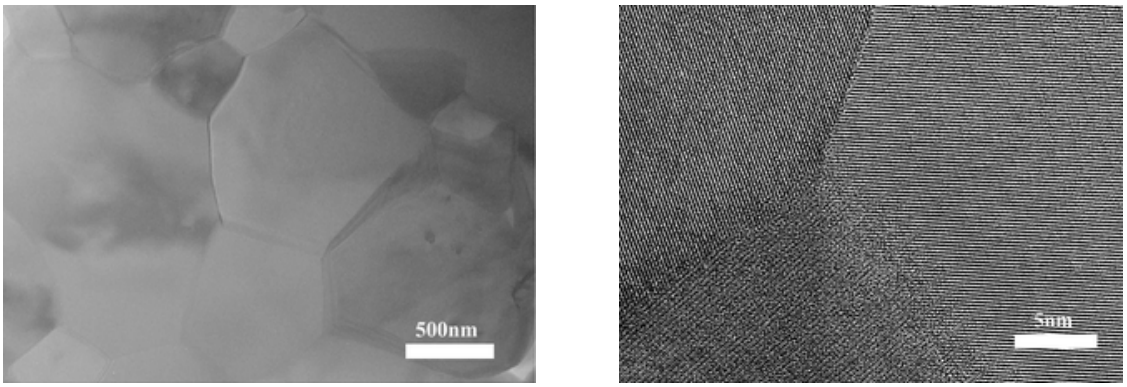

(a) TEM image of individual grains. (b) HRTEM image of grain boundaries.

Figure 2.1: TEM images of the microstructure of $BaZr_{0.95}Y_{0.05}O_{2.975}$ [31].

is called a grain boundary. Grain boundaries can exhibit different properties compared to the grain interior, as the structure of the grain boundary is different. The size, shape and density of grains in a material depend on a range of different aspects such as material properties (e.g., sinterability), fabrication methods and external conditions (temperature, pressure, etc.). As an example the microstructure of 5% yttrium-doped barium zirconate is shown in Fig. 2.1. Here the microstructure is dense with well-defined grains and grain boundaries.

The remainder of this chapter is divided into three sections. The first two gives a more detailed description of the structure of perovskite materials, where the crystal structure is the topic of Section 2.1 while grain boundaries are treated in Section 2.2. The last section deals with doping, which is the source for many material properties including conductivity in barium zirconate and other perovskites.

2.1 Crystal structure

Within the perovskite oxide family there exist many different crystal structures. The archetype is the cubic structure, which belongs to space group $Pm\bar{3}m$ and contains only one ABO_3 formula unit. This structure is depicted in Fig. 2.2. The A-site is located at the corners of the unit cell while the B-site is located at the center. The oxygen ions reside at the center of faces of the cell. The six oxygen ions form an octahedral unit with the B-site at the center (see Fig. 2.2). Other perovskite structures are obtained by reducing the symmetry of the cubic structure through distortion of one or several ions in the structure. Many of these structures consist of more than one ABO_3 formula unit in the primitive cell in order for the distor-

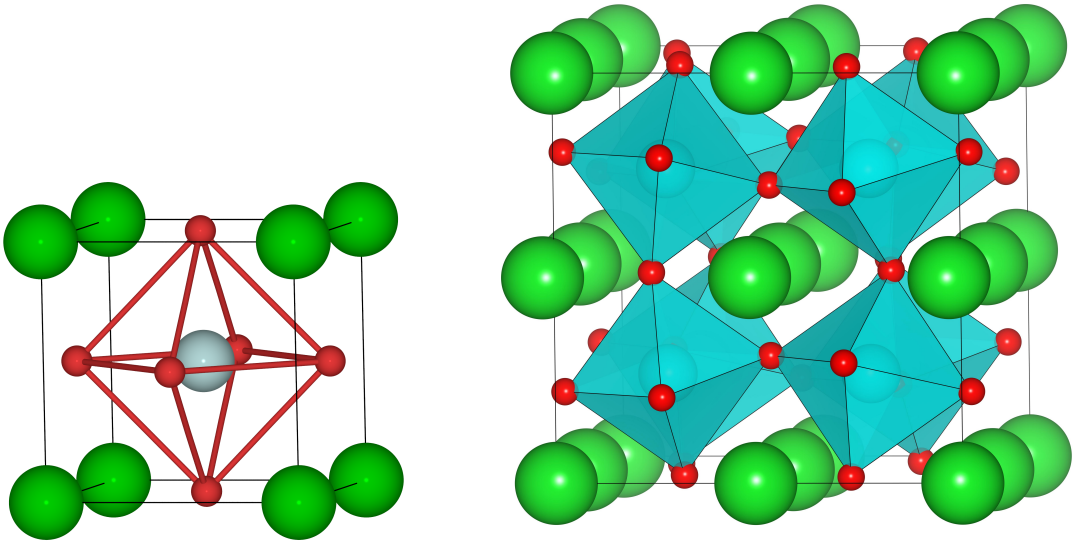

(a) Cubic structure.

(b) Distorted structure with octahedral tilting.

Figure 2.2: The perovskite lattice structure. Green, grey and red atoms indicate the A, B and oxygen site respectively.

tions to be made possible. A common distortion is tilting of the oxygen octahedra, which can occur both in and out of phase as well as in one or several directions. An example of such a structure is shown in Fig. 2.2. For a more detailed description and classification of these octahedral tilts see Ref. [32].

Distortions in the perovskite structure are associated with the size of the cations. Assuming that the ions are hard spheres with a radius r it follows from the cubic perovskite structure that

$$r_A + r_O = \sqrt{2}\left(r_B + r_O\right). \tag{2.1}$$

A distortion is more likely to occur if this conditions is violated. The *Goldschmidt tolerance factor* is a measure of the tendency to form distorted structures and is given by the ratio

$$t = \frac{r_A + r_O}{\sqrt{2}\left(r_B + r_O\right)} \tag{2.2}$$

where $t = 1$ yields the condition above and most likely corresponds to a cubic structure while larger and lower values are more prone to result in structures with reduced symmetry. More specifically, $t > 1$ is associated with a polar distortion of the B-site ion while $t < 1$ is associated with octahedral tilting [18]. Barium

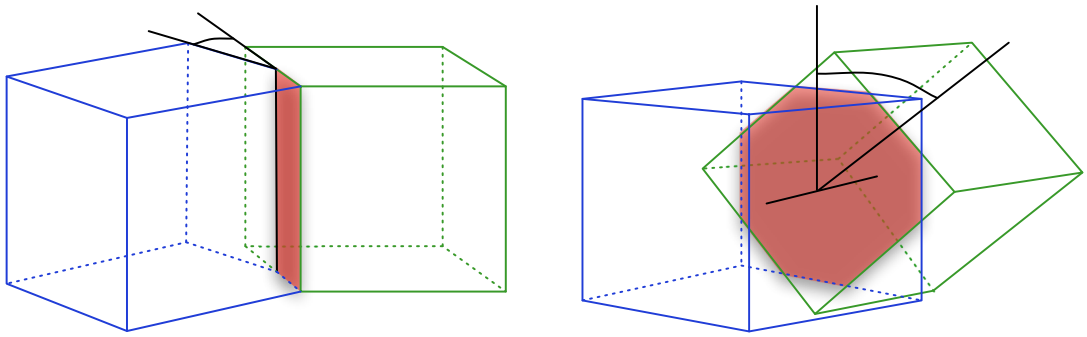

(a) Tilt boundary. (b) Twist boundary.

Figure 2.3: Schematic representation of a tilt and twist grain boundary.

zirconate has a tolerance factor close to 1 and forms in a cubic structure with a lattice constant in the range 4.191-4.197 Å [33, 34].

2.2 Grain boundaries

There are different types of grain boundaries in a material depending on the grain orientation. To understand grain boundary structures from a theoretical point it is convenient to start with a single crystal that is divided into two smaller crystals (or grains). A grain boundary can then be obtained by rotating one of the grains while keeping the other one fixed. A *tilt boundary* is obtained if the rotation occurs around an axis parallel to the interface while a *twist boundary* is obtained if the rotational axis is perpendicular to the interface. Fig. 2.3 shows a schematic representation of these grain boundary types. Grain boundaries in real materials generally contain both twist and tilt components.

Grain boundaries in acceptor-doped $BaZrO_3$ have been found to have low proton conductivity compared to the bulk of the material [10, 35–38]. As an example, Fig. 2.4 shows the proton conductivity of Y-doped $BaZrO_3$with a dopant content of 6%. The conductivity is several orders of magnitude lower at the grain boundaries compared to the bulk and the difference becomes more pronounced at lower temperatures. The low conductivity at boundaries determines the rate, and as a consequence, the total conductivity is lower compared to the bulk conductivity.

It has been concluded that the low grain boundary conductivity in $BaZrO_3$ is an intrinsic property since the grain boundaries do not contain any secondary phases [31, 39–41] (see Fig. 2.1). At present there are two explanations to the high grain boundary resistance in the literature, where one is more related to the proton mo-

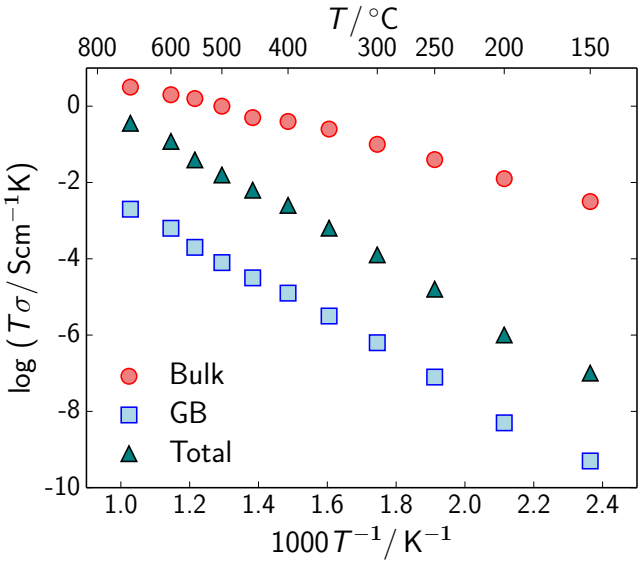

Figure 2.4: Total, bulk and grain boundary proton conductivity of 6% Y-doped $BaZrO_3$. The bulk and grain boundary conductivities are taken from [38]. The total conductivity is calculated based on the bulk and grain boundary contributions using a grain size of 1 µm.

bility while the other is related to the charge carrier concentration. The former argues that the structural disorder at the boundaries increases the migration barrier for proton diffusion, which reduce the mobility. First-principles studies of proton migration in grain boundaries in $BaZrO_3$ have indeed shown that migration barriers are larger at the grain boundary interface [42, 43].

The other explanation is the *space-charge model*. The premise of this model is that charged defects (protons and oxygen vacancies in $BaZrO_3$) accumulate at the grain boundary and give rise to an electrostatic potential. In turn, the potential depletes the surrounding regions of charge carriers, which reduces the conductivity. There is both experimental [31, 38, 41, 44–48] and theoretical [49, 50] evidence for space-charge formation at grain boundaries in $BaZrO_3$ in the literature. Theoretical results presented in Papers II-IV in this thesis give further evidence for this phenomenon. In a recent experimental study [51] the authors managed to impede space-charge formation in $BaZrO_3$ and obtain grain boundary activation energies comparable to that of the bulk by introducing a secondary phase of nickel at the grain boundaries. Space-charge formation at grain boundaries has also been seen in other perovskites, such as $SrTiO_3$ [52], $SrZrO_3$ [53] and $LaGaO_3$ [54, 55], as well as in other oxide materials, such as acceptor-doped CeO_2 and ZrO_2 [56].

2.3 Doping

It is common to tailor the properties of materials by the means of doping. This is no different for perovskite oxides. For instance, substituting an A or B-site cation with a dopant ion of a different size could change the crystal structure. If the dopant ion is aliovalent then the charge difference can be compensated by an increase in free charge carriers or the formation of charged defects. For $BaZrO_3$ (and many other perovskites) doping is a necessity when used as proton, oxide ion and electronic conductors. The conductivity is proportional to the charge carrier concentration and un-doped $BaZrO_3$ is an electrical insulator with a band gap of about 5 eV, and a poor ionic conductor due to low intrinsic defect concentrations. Acceptor doping is therefore used to improve the conductivity in this material.

More explicitly, the chemical formula for barium zirconate is $Ba^{2+}Zr^{4+}O_3^{2-}$. By substituting zirconium ions with dopant ions of a lower valence (M^{3+}) +2 charged oxygen vacancies are formed in order to maintain charge neutrality. In Kröger-Vink notation [57] this reaction reads as

$$2ZrO_2(s) + M_2O_3(s) \longrightarrow 2Zr_{Zr}^{\times} + 2M_{Zr}' + 5O_O^{\times} + V_O^{\bullet\bullet} \tag{2.3}$$

The associated charge neutrality condition is given by $2c_V = c_M$, where c_V and c_M denotes the oxygen vacancy and dopant concentration respectively. With an increase in the concentration of oxygen vacancies comes enhanced oxide ion conductivity since oxide ions diffuse through the vacancy mechanism (for more details regarding ionic diffusion see Section 4.1).

Oxygen vacancies are also important for the proton conductivity. Protons are introduced into the perovskite structure through the hydration of these vacancies. This reaction is given by

$$H_2O(g) + V_O^{\bullet\bullet} + O_O^{\times} \rightleftharpoons 2OH_O^{\bullet} \tag{2.4}$$

which describes how a water molecule hydrates the vacancy and forms two protons (hydroxide ions). It is also possible to introduce holes by oxidation of oxygen vacancies. This reaction is given by

$$\frac{1}{2}O_2(g) + V_O^{\bullet\bullet} \rightleftharpoons 2h^{\bullet} + O_O^{\times} \tag{2.5}$$

which describes the formation of holes at the expense of oxygen vacancies.

3

Point and planar defects

In theory, crystalline materials can be described by a perfect infinite structure of repeated primitive cells. This is never the case in reality, as defects, which break the symmetry, will always present in materials at finite temperatures. There exist a large number of different types of defects and these determine many properties of materials. This is the case for the electrical conductivity in perovskite oxides, which can be more explicitly described as diffusion of charged defects. Defects are a central part in all the appended papers in this thesis and most of the work done here can be described as the interplay between defects and the crystal structure.

The different varieties of defects can be categorized based on the extension of the defect in space. The ones with lowest dimension correspond to irregularities in the structure associated with single atoms and ions and these are referred to as point defects. There exist several different types of point defects. A *vacancy* is a lattice site without an atom and an *interstitial* defect is an atom located at position, which do not correspond to a lattice site. A *substitutional* defect refers to when an atom other then the original one of the host material occupies a lattice site. These three types of point defects are depicted in Fig. 3.1. Furthermore, the interstitial and the substitutional defects can be classified as either *intrinsic* or *extrinsic* depending on if the origin of the involved atom is of native or foreign character with respect to the host material. Defects of higher spatial dimension include line- (1D), planar- (2D) and bulk (3D) defects.

The purpose with this chapter is to present a theoretical framework for the modeling of point defects and to some extent also planar defects in the form of grain boundaries. These defects are specifically chosen since they play an important role for the proton conductivity in $BaZrO_3$. The chapter is organized in the following way. Sections 3.1-3.4 cover different aspects of point defect formation in bulk systems. Grain boundaries are then introduced in Section 3.5. The last section gives a

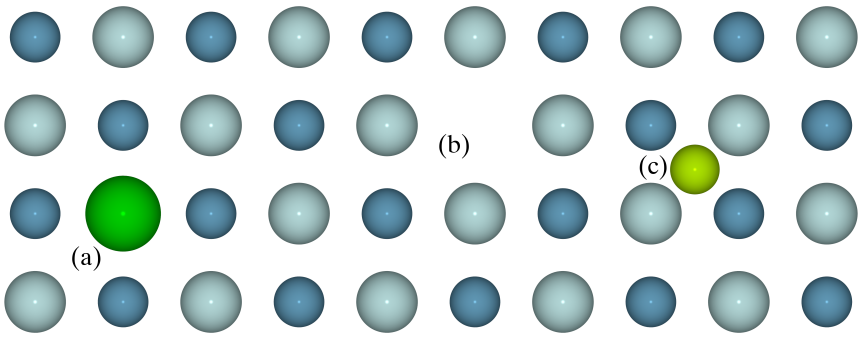

Figure 3.1: Schematic representation of point defects in a crystal lattice. Three defects are present: (a) a substitutional defect, (b) a vacancy and (c) an interstitial defect.

theoretical description of space-charge formation, which is a consequence of point defect formation in grain boundaries and other interfaces.

3.1 Chemical equilibrium

The formation of point defects is associated with a change in the Gibbs free energy which can be written as

$$\Delta G = \Delta H - T\Delta S \tag{3.1}$$

where ΔH and ΔS are changes in the enthalpy and entropy respectively, and T is temperature. It is convenient to separate ΔS into two parts

$$\Delta S = \Delta S^{\text{else}} + \Delta S^{\text{conf}} \tag{3.2}$$

where ΔS^{conf} specifically is the configurational contribution to the entropy while ΔS^{else} contains all other contributions. A general expression for the relation between the equilibrium concentration of a defect and the corresponding defect formation energy can be obtained by using Eq. 3.1 as a starting point. By assuming that n defects of an arbitrary species are formed on a discrete lattice, Eq. 3.1 can be written as

$$\Delta G = n\Delta H^{\text{f}} - Tn\Delta S^{\text{f}} - T\Delta S^{\text{conf}} = n\Delta G^{\text{f}} - T\Delta S^{\text{conf}} \tag{3.3}$$

where ΔH^{f} and ΔS^{f} is the change in enthalpy and entropy (not configurational entropy) upon formation of a single defect, and $\Delta G^{\text{f}} = \Delta H^{\text{f}} - T\Delta S^{\text{f}}$ is the corresponding free energy. Note that this expression is only valid under the condition

that the defects do not interact with each other. The configurational part of the entropy can be written as

$$\Delta S^{\text{conf}} = k \ln \Omega \tag{3.4}$$

where k is Boltzmann's constant and Ω is the multiplicity, which corresponds the number of possible ways to arrange the defects. If there are N available sites for the defects ($N > n$), where each site only can host one defect, then the multiplicity is given by

$$\Omega = \frac{N!}{n!\,(N-n)!} \tag{3.5}$$

By inserting this expression for Ω into Eq. 3.4 and taking use of Stirling's approximation[1], which is valid as both n and N are large numbers, the configurational entropy can be written as

$$\Delta S^{\text{conf}} = k \left(N \ln \frac{N}{N-n} - n \ln \frac{n}{N-n} \right) \tag{3.6}$$

It follows that the expression for ΔG in Eq. 3.3 can more explicitly be written as

$$\Delta G = n \Delta G^{\text{f}} - kT \left(N \ln \frac{N}{N-n} - n \ln \frac{n}{N-n} \right) \tag{3.7}$$

The total free energy of the defective system can be written as

$$G = G_0 + \Delta G \tag{3.8}$$

where G_0 is the free energy of the system without defects. In equilibrium G should be minimized with respect to n, which corresponds to

$$0 = \frac{\mathrm{d}G}{\mathrm{d}n} = \frac{\mathrm{d}}{\mathrm{d}n} (\Delta G) = \Delta G^{\text{f}} + kT \ln \frac{n}{N-n} \tag{3.9}$$

since G_0 is independent of n. At this point it is suitable to introduce the defect concentration c. By replacing n with c and N with $c^{\max}$, which is the maximum concentration, Eq. 3.9 can be written as

$$0 = \Delta G^{\text{f}} + kT \ln \frac{c}{c^{\max} - c} \tag{3.10}$$

From this expression it follows that the equilibrium concentration is given by

$$c = c^{\max} \frac{1}{1 + \exp\left(\Delta G^{\text{f}} / kT\right)} \tag{3.11}$$

For very low defect concentrations, which is often referred to as the *dilute limit*, $c \ll c^{\max}$ and Eq. 3.11 reduces to the more simple expression

$$c = c^{\max} \exp\left(-\frac{\Delta G^{\text{f}}}{kT} \right) \tag{3.12}$$

[1] $\ln x! \approx x \ln x - x$ for $x \gg 1$.

3.2 Law of mass action

The previous section showed that configurational entropy is a major driving force for point defect formation. This is however not the only mechanism and defect formation is often influenced by interactions. In a real material there are many different types of point defects, which can interact with each other and the environment. The energy associated with the addition or removal of a particle i in a certain environment is given by the chemical potential, which is defined as

$$\mu_i = \left(\frac{\partial G}{\partial n_i} \right)_{T,P,n_{j \neq i}} \tag{3.13}$$

With the same approach as in the previous section concerning the configurational entropy the chemical potential in a crystalline material can derived

$$\mu_i = \mu_i^\circ + kT \ln \frac{c_i}{c_i^{\max} - c_i} \tag{3.14}$$

where μ_i° is the chemical potential in a reference state. In the dilute limit this reduces to

$$\mu_i = \mu_i^\circ + kT \ln \frac{c_i}{c_i^{\max}} \tag{3.15}$$

A similar expression is obtained for the chemical potential of the constituents of an ideal gas:

$$\mu_i = \mu_i^\circ + kT \ln \frac{p_i}{p^\circ} \tag{3.16}$$

where p_i is the partial pressure and p° is the reference pressure.

Consider now the chemical reaction

$$n_\mathrm{A}\mathrm{A} + n_\mathrm{B}\mathrm{B} \rightleftharpoons n_\mathrm{C}\mathrm{C} + n_\mathrm{D}\mathrm{D} \tag{3.17}$$

where n_A, n_B, n_C and n_D corresponds to the number of species A, B, C and D respectively that takes part in the reaction. In equilibrium the free energy of the reactants (A and B) is equal to that of the products (C and D) which corresponds to

$$n_\mathrm{A}\mu_\mathrm{A} + n_\mathrm{B}\mu_\mathrm{B} = n_\mathrm{C}\mu_\mathrm{C} + n_\mathrm{D}\mu_\mathrm{D} \tag{3.18}$$

By substituting μ_i in this expression with the one in Eq. 3.15 followed by some rearrangements the *law of mass action* is obtained:

$$\frac{c_\mathrm{C}^{n_\mathrm{C}} c_\mathrm{D}^{n_\mathrm{D}}}{c_\mathrm{A}^{n_\mathrm{A}} c_\mathrm{B}^{n_\mathrm{B}}} = \exp\left(-\frac{\Delta G^\circ}{kT} \right) \equiv K \tag{3.19}$$

where $\Delta G^\circ = n_C\mu_C^\circ + n_D\mu_D^\circ - n_A\mu_A^\circ - n_B\mu_B^\circ$ and K is referred to as the equilibrium constant.

With the mass action law the equilibrium concentrations of the involved species can be obtained for any given reaction. A simple example for a reaction in oxides is the intrinsic defect reaction, which describes the formation of oxygen vacancies due to the reduction of oxygen. In Kröger-Vink notation [57] this reaction is given by

$$O_O^\times \rightleftharpoons \frac{1}{2}O_2(g) + V_O^{\bullet\bullet} + 2e' \tag{3.20}$$

with the corresponding equilibrium constant

$$K_{red} = \frac{c_V n_e^2 p_{O_2}^{1/2}}{c_O} \tag{3.21}$$

where c_V, n_e and c_O is the oxygen vacancy, electron and oxygen concentration respectively, and p_{O_2} is the oxygen partial pressure. If no other charged defects are present then the charge neutrality condition is given by $2c_V = n_e$. Site restriction on the oxygen sub-lattice gives $c_V + c_O = N_O$, where N_O is the concentration of oxygen sites. For small concentrations $c_V \ll N_O$ and thus is $c_O \approx N_O$. With these conditions the concentration of electrons and oxygen vacancies can be written as

$$n_e = 2c_V = \left(2N_O K_{red}\right)^{1/3} p_{O_2}^{-1/6} \tag{3.22}$$

More involved examples are the oxidation and hydration of oxygen vacancies in acceptor-doped perovskites. These materials contain +2 charged oxygen vacancies, which are formed to compensate the negatively charged acceptor dopants. The vacancies can then be hydrated or oxidized or both depending on the environmental conditions. These processes are described in more detail in Section 2.3. The equilibrium constant of the oxidation reaction in Eq. 2.5 is given by

$$K_{ox} = \frac{c_O n_h^2}{c_V p_{O_2}^{1/2}} \tag{3.23}$$

The site restriction in this case is the same as in the previous example but here is c_V no longer negligible since c_V is proportional to the dopant concentration, which could be quite substantial. The charge neutrality condition is given by $2c_V + n_h = c_A$ where the c_A denotes the dopant concentration. Since typically only a small fraction of the vacancies become oxidized n_h is negligible and the charge neutrality becomes $2c_V \approx c_A$. Based on these conditions the hole concentration can be written as

$$n_h = \left(\frac{c_A K_{ox}}{2N_O - c_A}\right)^{1/2} p_{O_2}^{1/4} \tag{3.24}$$

For the hydration reaction in Eq. 2.4 the equilibrium constant is given by

$$K_{\text{hydr}} = \frac{c_{\text{OH}}^2}{c_{\text{V}} c_{\text{O}} p_{\text{H}_2\text{O}}} \tag{3.25}$$

The site restriction now also includes the concentration of protons and is given by $c_{\text{OH}} + c_{\text{V}} + c_{\text{O}} = N_{\text{O}}$, and the charge neutrality condition reads as $2c_{\text{V}} + c_{\text{OH}} = c_{\text{A}}$ where the c_{A}. The proton concentration can then be written as

$$c_{\text{OH}} = N_{\text{O}} \frac{p_{\text{H}_2\text{O}} K_{\text{hydr}}}{p_{\text{H}_2\text{O}} K_{\text{hydr}} - 4} \left[1 - \sqrt{1 - \frac{p_{\text{H}_2\text{O}} K_{\text{hydr}} - 4}{p_{\text{H}_2\text{O}} K_{\text{hydr}}} \cdot \frac{c_{\text{A}}}{N_{\text{O}}} \left(2 - \frac{c_{\text{A}}}{N_{\text{O}}} \right)} \right] \tag{3.26}$$

3.3 Electronic defects

So far have electronic defects, electrons and holes in the conduction and valence band respectively, been treated in the same way as atomic defects within the mass action approach. Although the expressions for the electron and hole concentrations in the previous section (Eq. 3.22 and Eq. 3.24) are valid for the specific reactions, the general expression in Eq. 3.11 is not. Instead, the concentration of conduction band electrons and valence band holes in an insulator or semiconductor are given by

$$n_{\text{e}} = \int_{\varepsilon_{\text{cbm}}}^{\infty} g(\varepsilon) n_{\text{FD}}(\varepsilon) \mathrm{d}\varepsilon \tag{3.27}$$

$$n_{\text{h}} = \int_{-\infty}^{\varepsilon_{\text{vbm}}} g(\varepsilon) \left[1 - n_{\text{FD}}(\varepsilon) \right] \mathrm{d}\varepsilon \tag{3.28}$$

where ε_{vbm} and ε_{cbm} are the valence and conduction band-edges, $g(\varepsilon)$ is the density of states and $n_{\text{FD}}(\varepsilon)$ is the Fermi–Dirac distribution, which is given by

$$n_{\text{FD}}(\varepsilon) = \frac{1}{\exp\left[\left(\varepsilon - \mu_{\text{e}} \right) / kT \right] + 1} \tag{3.29}$$

where μ_{e} is the electron chemical potential.

The integrals in Eq. 3.27 and Eq. 3.28 can in general not be carried our analytically due to the complicated expressions for $n_{\text{FD}}(\varepsilon)$ and especially $g(\varepsilon)$. However, if the electron chemical potential is located well within the band gap with respect to kT then two approximations can be made, which makes the evaluation of the integrals much easier. First, in this case the Fermi–Dirac distribution reduces to the Boltzmann distribution, i.e.

$$n_{\text{FD}}(\varepsilon) \approx \exp\left(-\frac{\varepsilon - \mu_{\text{e}}}{kT} \right) \tag{3.30}$$

and a similar expression is obtained for $1 - n_{\mathrm{FD}}(\varepsilon)$ in Eq. 3.28. Second, the conduction electrons (and holes) can be assumed to behave as free particles with an effective mass m_{e} (m_{h}) which gives an explicit expression for $g(\varepsilon)$. With these two approximations the integrals can be solved analytically and following expressions for the concentrations can be obtained (see e.g., [58]):

$$n_{\mathrm{e}} = 2\left(\frac{2\pi m_{\mathrm{e}} kT}{h^2}\right)^{3/2} \exp\left(-\frac{\mu_{\mathrm{e}} - \varepsilon_{\mathrm{vbm}}}{kT}\right) = N_{\mathrm{e}} \exp\left(-\frac{\mu_{\mathrm{e}} - \varepsilon_{\mathrm{vbm}}}{kT}\right) \tag{3.31}$$

$$n_{\mathrm{h}} = 2\left(\frac{2\pi m_{\mathrm{h}} kT}{h^2}\right)^{3/2} \exp\left(-\frac{\varepsilon_{\mathrm{cbm}} - \mu_{\mathrm{e}}}{kT}\right) = N_{\mathrm{h}} \exp\left(-\frac{\varepsilon_{\mathrm{cbm}} - \mu_{\mathrm{e}}}{kT}\right) \tag{3.32}$$

where $\varepsilon_{\mathrm{vbm}}$ and $\varepsilon_{\mathrm{cbm}}$ correspond to the energy of the top of the valance band and the bottom of the conduction band respectively. Note that these expressions are similar to Eq. 3.12.

3.4 Free energy of defect formation

This section gives a short summary of the computational details regarding different contributions to the free energy of defect formation ΔG^{f}, which determines the defect concentration (see Eq. 3.11). A more detailed review of point defect modeling can be found in [59]. As defined in Eq. 3.3 the free energy of defect formation is given by

$$\Delta G^{\mathrm{f}} = \Delta H^{\mathrm{f}} - T\Delta S^{\mathrm{f}} \tag{3.33}$$

where it is important to remember that ΔS^{f} do not contain the configurational contribution to the entropy.

At zero temperature the free energy is given by

$$\Delta G^{\mathrm{f}}(0) = \Delta H^{\mathrm{f}}(0) = \Delta E^{\mathrm{f}}_{\mathrm{def}} + \Delta E^{\mathrm{zp}} \tag{3.34}$$

where $\Delta E^{\mathrm{f}}_{\mathrm{def}}$ is the electronic contribution and ΔE^{zp} is the change in zero-point energy upon forming the defect. The electronic contribution can be calculated according to

$$\Delta E^{\mathrm{f}}_{\mathrm{def}} = E^{\mathrm{tot}}_{\mathrm{def}} - E^{\mathrm{tot}}_{\mathrm{ideal}} - \sum_i \Delta n_i \mu^{\mathrm{el}}_i + q\mu_{\mathrm{e}} + E^{\mathrm{corr}} \tag{3.35}$$

where $E^{\mathrm{tot}}_{\mathrm{def}}$ and $E^{\mathrm{tot}}_{\mathrm{ideal}}$ is the electronic energy of the defective and ideal system respectively, Δn_i is the change in atomic species i upon forming the defect and μ^{el}_i is the corresponding electronic contribution to the chemical potential, q is the charge of the defect and μ_{e} is the electron chemical potential. The last term, E^{corr}, contains corrections for errors associated with charged defects, periodic boundary conditions, etc. and will be further discussed in Section 5.1.6.

Similar to Eq. 3.35, the free energy at finite temperatures and pressures can be written as

$$\Delta G^{\mathrm{f}}_{\mathrm{def}} = G^{\mathrm{tot}}_{\mathrm{def}} - G^{\mathrm{tot}}_{\mathrm{ideal}} - \sum_i \Delta n_i \mu_i + q\mu_{\mathrm{e}} + E^{\mathrm{corr}} \tag{3.36}$$

where $G^{\mathrm{tot}}_{\mathrm{def}}$, $G^{\mathrm{tot}}_{\mathrm{ideal}}$ and μ_i beside the electronic part now also include contributions that are related to the temperature and pressure. For the solid phase ($G^{\mathrm{tot}}_{\mathrm{def}}$, $G^{\mathrm{tot}}_{\mathrm{def}}$ and for some environments also μ_i) the vibrational contribution dominates and the free energy can be written as

$$G^{\mathrm{tot}}(T,P) = E^{\mathrm{tot}} + PV - F^{\mathrm{vib}}(T) \tag{3.37}$$

where V is the volume and $F^{\mathrm{vib}}(T)$ is the vibrational contribution. The PV-term is small for solids and is often neglected in practice. Within the harmonic approximation the vibrational free energy can be written as

$$F^{\mathrm{vib}}(T) = \sum_{\mathbf{q},s} \left\{ \frac{\hbar\omega_{\mathbf{q},s}}{2} + kT \ln\left[1 - \exp\left(-\frac{\hbar\omega_{\mathbf{q},s}}{kT}\right)\right] \right\} \tag{3.38}$$

where $\omega_{\mathbf{q},s}$ is the vibrational frequency for a specific wave vector $\mathbf{q}$ and band index s. The first term within the sum corresponds to the zero-point energy. For the gas phase the free energy follows a quite simple temperature and pressure dependence if the gas can be considered to be ideal. The chemical potential can then be written as

$$\mu(T,p) = \mu^{\mathrm{el}} + h(T) - Ts(T) + kT \ln \frac{p}{p^\circ} \tag{3.39}$$

where $h(T)$ and $s(T)$ is the enthalpy and entropy at the reference pressure p° and p is the partial pressure of the gas. Here $h(T)$ is defined in such a way that $h(0) = \varepsilon^{\mathrm{zp}}$, where $\varepsilon^{\mathrm{zp}}$ is the zero-point energy. $h(T)$ and $s(T)$ can for most gases be extracted from thermodynamic tables.

The electron chemical potential μ_{e} is determined by the charge neutrality condition, which states that the sum of all charges in the material should be equal to zero:

$$\sum_i q_i c_i(\mu_{\mathrm{e}}) + n_{\mathrm{h}}(\mu_{\mathrm{e}}) - n_{\mathrm{e}}(\mu_{\mathrm{e}}) = 0 \tag{3.40}$$

This equation can in general only be solved for μ_{e} numerically since there are often many different types defects present. However, in simple cases such as the reactions considered in Section 3.2 it is possible to find analytic expressions for μ_{e}.

3.5 Grain boundary formation and defect segregation

Unlike for point defects, the formation of grain boundaries is usually associated with an increase in free energy. This is due to that the configurational entropy, which is the driving force for point defect formation, is significantly smaller for grain boundaries and other defects of higher order [60]. Grain boundaries form as a consequence of the lattice mismatch between grains that occur during the growth of a crystal.

The increase in energy per area unit for a stoichiometric grain boundary can be determined according to

$$\gamma_{\mathrm{GB}} = \frac{G_{\mathrm{GB}} - G_{\mathrm{Bulk}}}{A} \tag{3.41}$$

where G_{GB} and G_{Bulk} is the free energy of a system with and without a grain boundary respectively, and A is the grain boundary area. For a non-stoichiometric boundary the expression for the interface energy becomes more complicated as it then also depends on the chemical potential of the constituent atoms.

As a consequence of that the structure is different at the grain boundaries the defect formation energies often differ there as well. The segregation energy of defect is defined as the difference in formation energy at or close to the boundary compared to the formation energy in the bulk:

$$\Delta G^{\mathrm{seg}} = \Delta G^{\mathrm{f}}_{\mathrm{def,GB}} - \Delta G^{\mathrm{f}}_{\mathrm{def,Bulk}} \tag{3.42}$$

where $\Delta G^{\mathrm{f}}_{\mathrm{def,GB}}$ and $\Delta G^{\mathrm{f}}_{\mathrm{def,Bulk}}$ can be determined according to Eq. 3.36. A common simplification, which is employed in Papers II-IV, is to assume that only the electronic contribution to the defect formation energy differs between the two configurations. The segregation energy is then given by

$$\Delta E^{\mathrm{seg}} = \Delta E^{\mathrm{f}}_{\mathrm{def,GB}} - \Delta E^{\mathrm{f}}_{\mathrm{def,Bulk}} = E^{\mathrm{tot}}_{\mathrm{def,GB}} - E^{\mathrm{tot}}_{\mathrm{def,Bulk}} \tag{3.43}$$

where $E^{\mathrm{tot}}_{\mathrm{def,GB}}$ and $E^{\mathrm{tot}}_{\mathrm{def,Bulk}}$ is the total energy of a supercell with a defect at the grain boundary and the bulk region respectively (cf. Eq. 3.35). Negative segregation energies indicate that it is more favorable to form defects at the interface while positive energies suggest the opposite. Negative segregation energies are the driving force for space-charge formation.

3.6 Space-charge modeling

The accumulation of charged defects in a material can give rise to space-charge formation, i.e. a charged region in space. As was discussed in Section 2.2, the

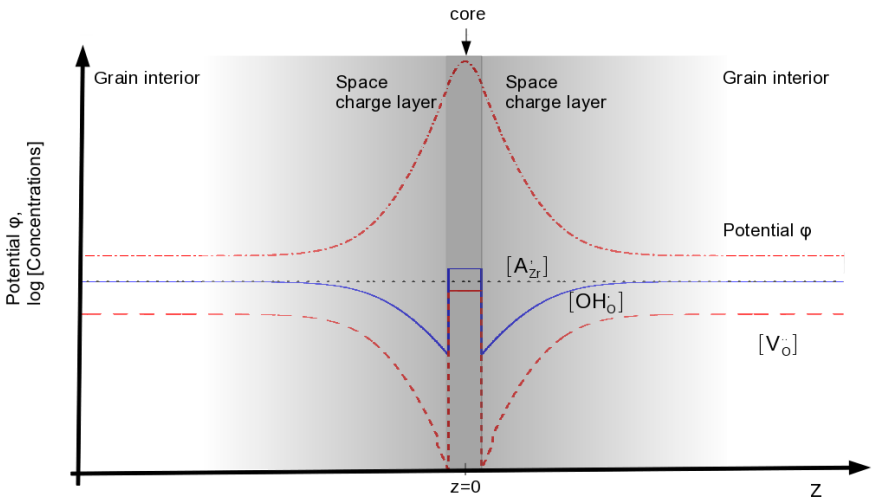

Figure 3.2: A schematic representation of a grain boundary within the space-charge model.

reduced proton conductivity at grain boundaries in $BaZrO_3$ is attributed to space-charge formation. A schematic representation of space charge formation at a grain boundary in $BaZrO_3$ is shown in Fig. 3.2. Charged oxygen vacancies ($V_O^{\bullet\bullet}$) and protons ($OH_O^{\bullet}$) segregate to the grain boundary, which increase the concentration of these defects at the grain boundary core (note the log scale in the figure). This results in a net charge which gives rise to an electrostatic potential. The potential depletes the surrounding regions, the space charge layers, of defects with the same charge, i.e. oxygen vacancies, protons and holes in this case. In turn, this reduces the conductivity across the boundary since the conductivity is proportional to the defect concentrations.

To describe the space-charge formation a theoretical model is needed. It is possible to derive a such model based on the *electrochemical potential*. In Sections 3.2 and 3.1 the chemical potential for a defect was derived on the basis of the configurational entropy. The same approach can be used to obtain the electrochemical potential for a defect of species i with charge q_i in an electrostatic potential φ, which is given by

$$\mu_i(x) = \mu_i^{\circ}(x) + q_i\varphi(x) + kT\ln\frac{c_i(x)}{c_i^{\max}(x) - c_i(x)} \tag{3.44}$$

where a one-dimensional spatial dependence (x) has been introduced. For a neutral defect this expression becomes equivalent to the expression for chemical potential in Eq. 3.14.

Assume that a grain boundary (or any other interface) is located at $x = 0$. Far from the boundary, at $x \approx \infty$, the system is in the bulk phase. In equilibrium the chemical potential of the should be the same everywhere and thus is

$$\mu_i(x) = \mu_i(\infty) \tag{3.45}$$

By substituting μ_i in this expression with Eq. 3.44 the following equation for the concentration is obtain.

$$\frac{c_i(x)}{c_i^{\max}(x) - c_i(x)} = \frac{c_i(\infty)}{c_i^{\max}(\infty) - c_i(\infty)} \exp\left(-\frac{\Delta\mu_i^\circ(x) + q_i\Delta\varphi(x)}{kT}\right) \tag{3.46}$$

where $\Delta\mu_i^\circ(x) = \mu_i^\circ(x) - \mu_i^\circ(\infty)$ is the segregation energy and $\Delta\varphi(x) = \varphi(x) - \varphi(\infty)$ is the space-charge potential. The space-charge potential can be obtained by solving Poisson's equation

$$\frac{\mathrm{d}^2}{\mathrm{d}^2 x}\left[\Delta\varphi(x)\right] = -\frac{1}{\varepsilon}\rho(x) \tag{3.47}$$

where ε is the dielectric function and $\rho(x)$ is the charge density, which given by

$$\rho(x) = \sum_i q_i c_i(x) \tag{3.48}$$

The set of coupled equations given by Eqs. 3.46-3.48 can be solved in an iterative, self-consistent manner in order to obtain equilibrium defect concentrations and the corresponding space-charge potential.

The space-charge model described above has been employed to $BaZrO_3$ in Paper II-IV. Paper II deals only with the segregation of oxygen vacancies while Paper III and IV also consider the segregation of protons. In all three papers the dopant concentration is assumed to be constant throughout the material, which is referred to as the *Mott-Schottky approximation* (see Fig. 3.2). In previous theoretical studies on space-charge formation the grain boundary core have been treated as a uniform region associated with one single segregation energy for each considered defect [49, 50, 52, 61]. Here the core is divided into layers where each layer contains one or several sites for each defect species. In turn, each site is associated with a segregation energy, which have been determined from first-principles (Paper III and IV) or interatomic potential (Paper II) calculations according to Eq. 3.43.

4

Conductivity

In general, the conductivity of a charge carrier is written as

$$\sigma = \frac{A}{T} \exp\left(-\frac{E_a}{kT}\right) \tag{4.1}$$

where A is a prefactor and E_a is the activation energy. There are many factors that influence these two quantities and these will be elucidated to some extent in this chapter.

There are two main properties of a charge carrier besides the charge that determines the conductivity: the *concentration* and the *mobility*. Under the assumption of non-interacting charge carriers the conductivity of a carrier i can be written as

$$\sigma_i = q_i B_i n_i \tag{4.2}$$

where n_i is the charge carrier concentration, B_i is the mobility and q_i is the charge. The previous chapter dealt with defects and the corresponding concentrations, both in bulk structures and at interfaces. This chapter will put more focus towards the other contributor to the conductivity, the carrier mobility.

The mobility of a charge carrier depends on several factors. Different carriers can have different conduction mechanisms depending on the nature of the carrier as well as the crystal structure of the material. For instance, the conduction mechanisms of protons and oxide ions in perovskites are different. Different structures within the same material (e.g., surfaces, interfaces and grain boundaries) could be associated with different mobilities compared to the bulk, which can lead certain conduction pathways through the material. There is also the possibility that defects in the material interact with the carrier, which may influence the mobility. One such example is that dopant ions have been found to act as trap sites

for protons in yttrium-doped $BaZrO_3$, which have a reducing effect on the proton conductivity [62].

The following two sections will consider the conduction mechanisms of the charge carriers that are relevant for a large set of acceptor-doped perovskites, including $BaZrO_3$. The first one will discuss ionic conduction with emphasis on oxide ions (oxygen vacancies) and protons while the second covers electron and hole conduction. The text that follows is just a short summary of the topic. A more detailed theoretical description can be found in textbooks on the subject such as [60, 63].

4.1 Ionic conduction

The mobility of an ion is related to the self-diffusion coefficient D through the Nernst-Einstein relation [64]

$$B = \frac{qD}{kT} \tag{4.3}$$

where k is Boltzmann's constant and T is the temperature. By assuming that ionic diffusion in a material resembles that of a three-dimensional random walk the diffusion coefficient can be written as

$$D = \alpha Z N_s \nu \exp\left(-\frac{\Delta G^m}{kT}\right) = \alpha Z N_s \nu \exp\left(\frac{\Delta S^m}{k}\right) \exp\left(-\frac{\Delta H^m}{kT}\right) \tag{4.4}$$

where Z is the number of adjacent sites the ion can move into, N_s is the fraction of the adjacent sites that are empty, ν is an attempt frequency which represent how often the ion tries to move away from the current site and $\Delta G^m = \Delta H^m - T\Delta S^m$ is the free energy of migration. Finally, α is a factor that includes several contributions: geometric considerations such as lattice structures and constants, as well as a correlation factor which accounts for non-randomness in the diffusion. In perovskites both oxide ions and protons diffuse on the oxygen sub lattice, although though different mechanisms, and thereby does Z correspond to the number of neighboring oxygen ions.

The nature of the diffusion mechanism is reflected in N_s. For oxide ions it is only possible to move to a nearby vacant site and thereby does N_s correspond to the fractional concentration of oxygen vacancies in the material, which can be written as $N_s = c_V/N_O$ where c_V and N_O is the concentration of vacancies and oxygen lattice sites respectively. A schematic picture of this conduction mechanism is shown in Fig. 4.1. As the oxide ion moves into a vacant site the initial site becomes empty. Thus, instead of having an oxide ion moving in one direction, it can be thought of as if the oxygen vacancy is the diffusing species, moving in the opposite direction. This view is more common as the concentration of vacancies is in most cases much smaller than the concentration of oxide ions.

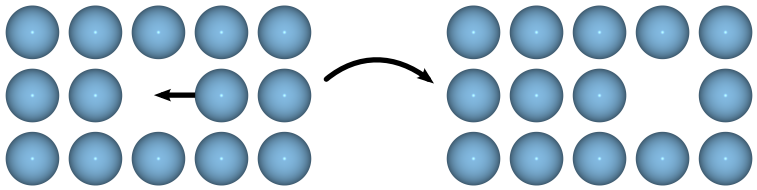

Figure 4.1: A schematic representation of the vacancy diffusion mechanism. The missing ion corresponds to the vacancy. When the ion moves to the left the vacancy moves in the opposite direction to the right.

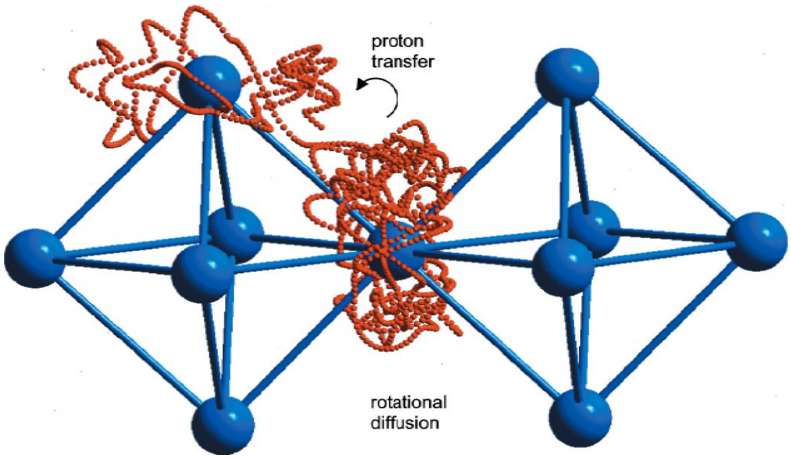

Figure 4.2: Proton trajectory that shows the two steps of the proton diffusion mechanism: rotation and transfer. Figure from Ref. [10].

Like oxygen vacancies, protons in perovskite oxides also diffuse on the oxygen sub lattice, although through completely different mechanism. When introduced into the material (see Eq. 2.4) the proton bonds with a nearby oxygen and forms a hydroxide ion. The proton can then move around on the oxygen sub lattice through a two-step Grotthuss mechanism [65, 66]. The proton can rotate around the oxide ion and transfer between two adjacent oxide ions. A proton trajectory displaying these two steps is shown in Fig. 4.2. As the proton moves from one oxide ion to another the number of available sites for diffusion is given by $N_s = c_O/N_O$, where c_O is the oxide ion concentration.

By combing Eq. 4.2, 4.3 and 4.4 together with the expression for N_s the conductivity of both oxygen vacancies and protons can be written as

$$\sigma_i = \frac{q_i^2 c_i \alpha Z \nu_i \exp\left(\Delta S_i^m/k\right)}{kT} \exp\left(-\frac{\Delta H_i^m}{kT}\right) \tag{4.5}$$

where the assumption is made that $c_O/N_O \approx 1$, which is reasonable for most systems. At first glance, comparing this expression with Eq. 4.1 would suggest that the activation energy is completely given by the migration barrier. This is true if the defect concentration is fixed. However, this is not always the case, which was shown in the previous chapter, and in many cases the concentration follows an exponential temperature dependence. In the dilute limit the concentration is given by Eq. 3.12 and Eq. 4.5 can then be written as

$$\sigma_i = \frac{q_i^2 c_i^{\max} \alpha Z \nu_i \exp\left[\left(\Delta S_i^{\mathrm{m}} + \Delta S_i^{\mathrm{f}}\right)/k\right]}{kT} \exp\left(-\frac{\Delta H_i^{\mathrm{m}} + \Delta H_i^{\mathrm{f}}}{kT}\right) \tag{4.6}$$

Comparing this expression with Eq. 4.1 indicate that

$$E_a = \Delta H_i^{\mathrm{m}} + \Delta H_i^{\mathrm{f}} \tag{4.7}$$

which means that the activation energy depends both on the migration barrier and the defect formation energy. More complicated expressions for the concentrations, such as Eq. 3.22 and Eq. 3.26, depend on the equilibrium constant and consequently does the free energy of the corresponding reaction enter into the activation energy. Additionally, these expressions follow a non-exponential dependence on external parameters such the partial pressures and dopant concentrations, which then enters into the prefactor.

4.2 Electronic conduction

Similar to the activated diffusion of ions (Eq. 4.3 and Eq. 4.4) the mobility of electron and holes can be written as

$$B = B_0(T) \exp\left(-\frac{\Delta H^{\mathrm{m}}}{kT}\right) \tag{4.8}$$

where the prefactor $B_0(T)$ contains all contributions the mobility except the migration barrier. For free carriers (band-states) there is no migration barrier ($\Delta H^{\mathrm{m}} = 0$) and the mobility corresponds to the prefactor $B_0(T)$, where $B_0(T) \sim T^{-3/2}$ if the scattering of electrons is only due to phonons [60].

In many metal oxides including perovskites the motion of electrons and holes is not free since the electronic carriers interact with the lattice. The electrons and holes polarize the environment and the charge carrier together with the associated lattice distortion is called a *polaron*. There are two main types of polarons: large and small (localized). For a large polaron the interaction between the electron or hole and the lattice is weak and the conduction mechanism is similar to that of free carriers. The large polaron mobility is associated with a small, finite migration

barrier and $B_0(T) \sim T^{-1/2}$. For small polarons the interaction with the lattice is much stronger. The conduction mechanism is in this case very similar to ionic conduction with thermally activated jumps.

5

Computational methods

A theoretical description of matter is essential in order to understand the structural and chemical properties of materials. On the atomic scale, any property of a system of interacting particles should be possible to obtain from the corresponding quantum mechanical wave function $\Psi(\mathbf{r}_1, \mathbf{r}_2, \ldots, \mathbf{R}_1, \mathbf{R}_2, \ldots; t)$, where $\mathbf{r}_i$ and $\mathbf{R}_I$ denotes the position of electron i and nucleus I respectively while t is time. The wave function can in principle be obtained by solving the time independent Schrödinger equation

$$H\Psi_n(\mathbf{r}_1, \mathbf{r}_2, \ldots, \mathbf{R}_1, \mathbf{R}_2, \ldots) = E_n\Psi_n(\mathbf{r}_1, \mathbf{r}_2, \ldots, \mathbf{R}_1, \mathbf{R}_2, \ldots) \tag{5.1}$$

where the Hamiltonian of the system is given by (in atomic units[1])

$$\begin{aligned} H = &-\frac{1}{2}\sum_i \nabla_i^2 + \frac{1}{2}\sum_{i\neq j}\frac{1}{|\mathbf{r}_i - \mathbf{r}_j|} - \sum_{i,I}\frac{Z_I}{|\mathbf{r}_i - \mathbf{R}_I|} \\ &-\frac{1}{2}\sum_I \frac{\nabla_I^2}{M_I} + \frac{1}{2}\sum_{I\neq J}\frac{Z_I Z_J}{|\mathbf{R}_I - \mathbf{R}_J|} \end{aligned} \tag{5.2}$$

where M_I and Z_I denotes the mass and charge of the nuclei. The first and fourth term on the right-hand side of Eq. 5.2 corresponds to the kinetic energy of the electrons and the nuclei respectively, while the other three terms corresponds to Coulombic interactions. To solve Eq. 5.1 is an extremely difficult task and an exact solution is only possible to obtain for small systems such as single atoms or small molecules. Most problems of interest are associated with much larger system sizes and approximations are therefore needed in order to pursue such problems.

A first approximation that is the starting point for many methods is that the electrons and the nuclei can be treated separately. This is possible since the nuclei

[1] $\hbar = e = m_e = 4\pi\varepsilon_0 = 1$

are much heavier compared to the electrons and as a consequence the electron dynamics is much faster. In many situations it is therefore reasonable to assume that the electrons can relax into the ground state of any given atomic configuration. This is called the Born-Oppenheimer approximation [67].

The Hamiltonian of the electronic problem is given by

$$H_{\mathrm{e}} = -\frac{1}{2}\sum_i \nabla_i^2 + \frac{1}{2}\sum_{i\neq j}\frac{1}{|\mathbf{r}_i - \mathbf{r}_j|} + V_{\mathrm{ext}} \tag{5.3}$$

where V_{ext} is the external potential from the nuclei. Solving the Schrödinger equation for the electrons is still a formidable problem, and more approximations are needed to obtain a solution. The following sections (Section 5.1-5.3) describe three different approaches to solve this equation at different levels of approximations and accuracy.

The nuclear problem is often approached with the assumption that the quantum mechanical effects are quite small and it is therefore reasonable to consider a classical treatment of the nuclei. Furthermore, The Hellmann-Feynman theorem [68] yields the following simple relation between the force exerted on a nucleus and the total energy E of the ion-electron system

$$\mathbf{F}_I = -\frac{\partial E}{\partial \mathbf{R}_I} \tag{5.4}$$

The forces can be used in minimization schemes to find ground state structures or in Newton's equation of motion to study dynamical properties.

5.1 Density-functional theory

Density-functional theory (DFT) is a first-principles method which revolves around the electron density $n(\mathbf{r})$. It can be shown (see Section 5.1.1) that if the ground state density is known then everything about the ground state is known. The density is obtained by integrating the electronic wave function over all coordinates except one:

$$n(\mathbf{r}) = \int \dots \int \Psi^*(\mathbf{r}, \mathbf{r}_2, \dots, \mathbf{r}_N)\Psi(\mathbf{r}, \mathbf{r}_2, \dots, \mathbf{r}_N)\mathrm{d}\mathbf{r}_2 \dots \mathrm{d}\mathbf{r}_N \tag{5.5}$$

Thus, for a system with N electrons, by considering the electron density instead of the corresponding wave function the degrees of freedom in the system are reduced from $3N$ to 3. This results in a much more tractable problem.

Modern DFT relies upon a theoretical framework, which was derived by Walter Kohn and coworkers in the 1960s, for which he was awarded the Nobel Prize in Chemistry in 1998. A short summary of this theory is described in the following sections, with emphasis on extended systems. For a more thorough description of DFT, see e.g., [69**?** –71].

5.1.1 The Hohenberg-Kohn theorems

In 1964 Hohenberg and Kohn [72] formulated and proved two theorems that make up the foundation of modern DFT. What they essentially state is that Eq. 5.5 can be reversed for the ground state density: if the ground state density $n_0(\mathbf{r})$ is known then so is the ground state wave function $\Psi_0(\mathbf{r}, \mathbf{r}_2, \ldots, \mathbf{r}_N)$ and consequently all ground state properties.

The first theorem states that the non-degenerate ground state wave function is a unique functional of the ground state density: $\Psi_0(\mathbf{r}_1, \mathbf{r}_2, \ldots, \mathbf{r}_N) = \Psi[n_0(\mathbf{r})]$. It follows that the ground state expectation value of any observable, including the ground state energy E_0, is a functional of $n_0(\mathbf{r})$ as well,

$$E_0 = E[n_0(\mathbf{r})] = \langle \Psi[n_0(\mathbf{r})] \big| H_\mathrm{e} \big| \Psi[n_0(\mathbf{r})] \rangle \tag{5.6}$$

The second theorem states that there exists a functional for the energy of the form

$$E[n(\mathbf{r})] = F[n(\mathbf{r})] + \int n(\mathbf{r}) V_\mathrm{ext}(\mathbf{r}) \mathrm{d}\mathbf{r} \tag{5.7}$$

which is minimized by the ground state density. $F[n(\mathbf{r})]$ contains the contributions from the kinetic energy and the electron-electron interactions. The functional is variational and the minimum corresponds to the ground state energy:

$$E[n_0(\mathbf{r})] \leq E[n(\mathbf{r})] \tag{5.8}$$

Even if the problem has been simplified to finding the minimum of a functional with respect to a 3-dimensional function instead of solving the $3N$-dimensional system $\langle \Psi_0(\{\mathbf{r}_i\}) \big| H_\mathrm{e} \big| \Psi_0(\{\mathbf{r}_i\}) \rangle$ it is still a difficult problem to solve. The reason for this is that the functional $F[n(\mathbf{r})]$ contains complex many-body effects, of which exact representation is not known.

5.1.2 The Kohn-Sham equations

In 1965 Kohn and Sham [73] derived a scheme that makes it possible to determine the ground state density and the corresponding energy. The key concept with this scheme is that a system consisting of *interacting* electrons can be transformed into a system with *non-interacting* electrons, which much easier to solve. In practice, this is done by writing $F[n(\mathbf{r})]$ of non-interacting electrons on the form

$$F[n(\mathbf{r})] = T_\mathrm{s}[n(\mathbf{r})] + E_\mathrm{H}[n(\mathbf{r})] + E_\mathrm{xc}[n(\mathbf{r})] \tag{5.9}$$

where $T_\mathrm{s}[n(\mathbf{r})]$ is the kinetic energy of non-interacting electrons, $E_\mathrm{H}[n(\mathbf{r})]$ is the Hartree energy which is given by

$$E_\mathrm{H}[n(\mathbf{r})] = \frac{1}{2} \iint \frac{n(\mathbf{r}) n(\mathbf{r}')}{|\mathbf{r} - \mathbf{r}'|} \mathrm{d}\mathbf{r} \mathrm{d}\mathbf{r}' \tag{5.10}$$

and $E_{xc}[n(\mathbf{r})]$ is the exchange and correlation energy which contains the complicated many-body effects. Based on this expression for $F[n(\mathbf{r})]$, the interacting electrons can be treated as non-interaction electrons moving in an effective potential given by

$$V_{eff}(\mathbf{r}) = V_{ext}(\mathbf{r}) + V_H(\mathbf{r}) + V_{xc}(\mathbf{r}) \tag{5.11}$$

where $V_H(\mathbf{r})$ is the Hartree potential

$$V_H(\mathbf{r}) = \int \frac{n(\mathbf{r}')}{|\mathbf{r} - \mathbf{r}'|} d\mathbf{r}' \tag{5.12}$$

and $V_{xc}(\mathbf{r})$ is the exchange-correlation potential which corresponds to the functional derivate of $E_{xc}[n(\mathbf{r})]$:

$$V_{xc}(\mathbf{r}) = \frac{\delta E_{xc}[n(\mathbf{r})]}{\delta n(\mathbf{r})} \tag{5.13}$$

This gives rise to the Kohn-Sham equations, which is a set of Schrödinger equations for non-interacting electrons that are coupled through the electron density:

$$\left[-\frac{1}{2}\nabla^2 + V_{eff}(\mathbf{r})\right] \psi_i(\mathbf{r}) = \varepsilon_i \psi_i(\mathbf{r}) \tag{5.14}$$

where the density is given by

$$n(\mathbf{r}) = \sum_i f_i \left|\psi_i(\mathbf{r})\right|^2 \tag{5.15}$$

and where f_i is the occupation of the electron state corresponding to $\psi_i(\mathbf{r})$. Since the single particle wave functions $\psi_i(\mathbf{r})$ depend on $V_{eff}(\mathbf{r})$ which in turn depends on $n(\mathbf{r})$ these equations have to be solved iteratively until a self-consistent solution is obtained. The solution corresponds to the ground state density $n_0(\mathbf{r})$ and based on that the ground state energy is determined according to

$$E_0 = \sum_i f_i \varepsilon_i + E_{xc}[n_0(\mathbf{r})] - \int V_{xc}(\mathbf{r}) n_0(\mathbf{r}) d\mathbf{r} - \frac{1}{2} \iint \frac{n_0(\mathbf{r}) n_0(\mathbf{r}')}{|\mathbf{r} - \mathbf{r}'|} d\mathbf{r} d\mathbf{r}' \tag{5.16}$$

The Kohn-Sham approach simplifies the problem significantly but no approximations have yet been made and to find the exact solution is still a difficult problem. This due to that $E_{xc}[n(\mathbf{r})]$ is defined by Eq. 5.9 and since $F[n(\mathbf{r})]$ is unknown then so is $E_{xc}[n(\mathbf{r})]$. As a result, $E_{xc}[n(\mathbf{r})]$ contains contributions from all the complex many-body effects as well. Thus, approximations of $E_{xc}[n(\mathbf{r})]$ are needed in order to proceed any further. This is the topic of the next section.

Additionally, spin is not included here but the Kohn-Sham equations can be easily be generalized to include this, which is necessary to describe certain systems properly (e.g., magnetic systems).

5.1.3 Exchange-correlation functionals

Many approximations of the exchange-correlation functional have been suggested over the years with varying level of complexity. The most simple approximation is the *local density approximation* (LDA) which was proposed by Kohn and Sham in their original paper [73]. Within this approximation the exchange-correlation energy is given by

$$E_{\mathrm{xc}}^{\mathrm{LDA}}[n(\mathbf{r})] = \int n(\mathbf{r})\varepsilon_{\mathrm{xc}}^{\mathrm{LDA}}[n(\mathbf{r})]\mathrm{d}\mathbf{r} \tag{5.17}$$

where $\varepsilon_{\mathrm{xc}}^{\mathrm{LDA}}(n(\mathbf{r}))$ is the exchange-correlation energy density of a uniform electron gas with density $n(\mathbf{r})$. In spite of its simplicity, this approximation works remarkably well for a wide range of materials and properties.

The electron density of most materials is inhomogeneous and a natural next step beyond LDA is to take variations in the density into account. The practical approach is the semi-local *generalized gradient approximation* (GGA), which beside the density also takes the gradient of the density into account:

$$E_{\mathrm{xc}}^{\mathrm{GGA}}[n(\mathbf{r})] = \int n(\mathbf{r})\varepsilon_{\mathrm{xc}}^{\mathrm{GGA}}[n(\mathbf{r}), \nabla n(\mathbf{r})]\mathrm{d}\mathbf{r} \tag{5.18}$$

The gradient can be incorporated in many different ways and there exists a wide range of different GGAs. There are two different main approaches to obtain GGA functionals: derivations based on theoretical arguments and fitting parameters to reproduce experimental results of desired properties. The GGA functional PBE [74] is of the former kind and is one of the most popular functionals for calculations of materials. This functional has been employed in Papers I, III and IV in this thesis. Empirically fitted functionals are more frequently used in quantum chemistry. The GGAs improve on LDA in many aspects, such as cohesive energies and bond lengths, however, there are some systems and properties that are better described with LDA.

The functionals that have been discussed so far are only a few of all the ones available in the literature. While the standard functionals (LDA and GGA) manage to reasonably predict many properties they systematically fail in some cases, such as obtaining chemical accuracy and describing van der Waals interactions. For many cases it is possible to decrease errors by tuning the functional in different ways. There are however errors that are inherent to the approximations themselves and these are not as easy to reduce. This is the case for the band gap of semiconductors and insulators, which is severely underestimated by both LDA and GGA. This is the topic of the next section.

5.1.4 The band gap problem

It is well known that LDA and GGA functionals systematically underestimates the band gap of semiconductors and insulators by up to about 40-50%, and this is referred to as the *band gap problem* of DFT. For instance, the experimental band gap of $BaZrO_3$ is around 5 eV while PBE predicts a band gap of about 3 eV (see Paper I). The origin of the band gap problem is twofold. One aspect is related to a discontinuity in the exchange-correlation functional while the other is due to a self-interaction error.

The fundamental band gap of an insulator or semiconductor is given by

$$E_{\text{gap}} = I - A \tag{5.19}$$

where I is the ionization energy and A is the electron affinity. Within DFT this equation can be written in terms of the derivative of the Kohn-Sham functional

$$E_{\text{gap}} = \frac{\delta E}{\delta n}\Big|_{N+\delta} - \frac{\delta E}{\delta n}\Big|_{N-\delta} \tag{5.20}$$

where N is the number of electrons and $\delta \to 0$. This expression indicates that the band gap originates from a derivate discontinuity in the functional. In fact, it has been shown [76] that for the exact Kohn-Sham functional the slope of the total energy $E(N)$ is a straight line with discontinuities at integer values of N. For the exact functional Eq. 5.20 yields

$$E_{\text{gap}} = \varepsilon_{\text{gap}} + \Delta_{\text{xc}} \tag{5.21}$$

where ε_{gap} is the band gap from the Kohn-Sham energy spectrum and Δ_{xc} is the derivative discontinuity in the xc-functional:

$$\Delta_{\text{xc}} = \frac{\delta E_{\text{xc}}}{\delta n}\Big|_{N+\delta} - \frac{\delta E_{\text{xc}}}{\delta n}\Big|_{N-\delta} = V_{\text{xc}}\big|_{N+\delta} - V_{\text{xc}}\big|_{N-\delta} \tag{5.22}$$

While ε_{gap} stems from the kinetic energy of the non-interacting particles (T_{s} in Eq. 5.9), which is exact, Δ_{xc} depends on the approximation of E_{xc} and varies accordingly. V_{xc} is continuous for LDA and GGA functionals and consequently is $\Delta_{\text{xc}} = 0$. This yields the first contribution to the underestimation of the band gap since $\Delta_{\text{xc}} > 0$ for the exact functional [77–79].

The second part of the band gap error is due to the Hartree term (Eq. 5.10), which introduces a spurious self-interaction. While the exact xc-functional cancels this error this is not the case for LDA and GGA. The effect of the self-interaction error is that delocalization becomes favorable, which has a severe impact on highly localized electron orbitals, those representing *d*- and *f*-electrons. This is embodied

in the $E(N)$-curve, which for LDA and GGA becomes convex between integer values of N, in contrast to the straight line of the exact Kohn-Sham functional, and therefore incorrectly describes fractional charges [80].

Different approaches have been proposed to remedy the band gap problem. In Paper I two different methods have been used to improve the band gap of $BaZrO_3$: a *hybrid functional* and the G_0W_0 method (see Section 5.2). Hybrid functionals [81–83] are a class of functionals which substitutes a part of the DFT exchange with Hartree-Fock (HF) [84] exchange, giving an exchange-correlation functional of the form

$$E_{\mathrm{xc}}^{\mathrm{hybrid}} = E_{\mathrm{xc}}^{\mathrm{DFT}} + \alpha \left(E_{\mathrm{x}}^{\mathrm{HF}} - E_{\mathrm{x}}^{\mathrm{DFT}} \right) \tag{5.23}$$

where α is a mixing parameter. The motivation for this approach is that HF systematically overestimates the band gap due to a localization error, which is related to that the $E(N)$-curve is concave [80], and by combining the two methods the corresponding errors are expected to cancel to a large extent thus leading to a more accurate estimation of the band gap. The mixing parameter α is treated differently with different hybrid functionals. With the PBE0 functional, which was used in Paper I, $\alpha = 0.25$ which is based on theoretical arguments [85]. This is also the case for the HSE functional [86, 87], which also contains a screening parameter ω that determines the range of the HF exchange in order to reduce the computational effort. However, in recent years there have been many studies based on the HSE functional where α and ω have been treated as free parameters and they are often fitted to reproduce certain properties such as experimental band gaps.

5.1.5 Plane waves and pseudopotentials

Finding a solution to the Kohn-Sham equations in a practical calculation requires further considerations. First, a mathematical representation of the single particle wave functions is needed. There are many possible representations and a suitable choice depends on the system under consideration. For solid systems it is convenient to expand the wave function in a plane wave basis and to employ periodic boundary conditions, due to the periodic nature of the crystal structure. Systems without periodicity, such as defects, can still be treated using the supercell approach. The use of periodic boundary conditions results in an infinite system but by utilizing Bloch's theorem [88] the complete basis for the wave function can be obtained by considering only the wave vectors $\mathbf{k}$ within the first Brillouin zone. The basis functions can then be written as a Fourier series

$$\psi_{n,\mathbf{k}}(\mathbf{r}) = \sum_{\mathbf{G}} c_{n,\mathbf{k}+\mathbf{G}} \exp\left[i\left(\mathbf{k}+\mathbf{G}\right)\cdot\mathbf{r}\right] \tag{5.24}$$

where the sum is over all reciprocal lattice vectors $\mathbf{G}$ and n denotes the band index. Since there is an infinite set of $\mathbf{G}$ vectors this sum has to be truncated in order to

be evaluated numerically. This is done by introducing a cut off energy E_{cut} which limits the number of $\mathbf{G}$ vectors according to $\frac{1}{2}|\mathbf{k}+\mathbf{G}|^2 < E_{\text{cut}}$.

While the use of plane waves simplifies the problem substantially a drawback with this method is the slow convergence for rapidly oscillating wave functions near the nuclei. However, the core electrons do not take part in chemical bonding and they can therefore be treated differently compared to the valence electrons. Additionally, a good description of the valence electrons near the nuclei is not crucial for obtaining a proper solution. For these reasons it is common to replace the potential arising from the nuclei and the core electrons with an effective potential which is referred to as a *pseudopotential*. The pseudopotential is constructed in such a way that it produces a more smooth function within the core region which requires a lower cut off energy, while it reproduces the all-electron wave function outside the core region. Pseudopotentials makes the calculations less computationally demanding since only the valence electrons are treated explicitly. There is no restricted form for pseudopotentials as long as certain conditions are required. This has allowed for different implementations such as norm-conserving pseudopotentials [89], ultrasoft pseudopotentials [90] and the projector augmented wave method (PAW) [91]. The latter has been employed for all DFT calculations in this thesis.

5.1.6 Correction schemes

Periodic boundary conditions are very suitable for modeling periodic structures such as ideal crystals. However, problems arise for a non-periodic system, which is the case when modeling e.g., a surface, an interface or a single point defect. The periodic boundary conditions imply an infinite array of supercells, which introduce spurious interactions between the defective structure and its periodic images. The magnitude of these interactions has an inverse dependence on the distance. Thus, a first step to limit these interactions and to reduce associated errors is to increase the size of the supercell. This can only be done up to a certain point since DFT is limited to relatively small system sizes, and additional corrections may therefore have to be employed in order to obtain accurate results. This is important especially for charged systems due to the long-range Coulomb interactions, which decay slowly as L^{-1}, where L is the length of the supercell.

A theoretical description of finite size corrections is most easily derived for point defects in a cubic lattice. There are two main types of spurious interactions: *electrostatic* and *elastic*. These interactions typically scale as L^{-1} and L^{-3} and a simple correction is to extrapolate to an infinite system using a fitted polynomial on the form [92, 93]

$$E(L) = E_\infty + aL^{-1} + bL^{-3} \tag{5.25}$$

The main drawback with the extrapolation is that it requires calculations for several different values for L, which can be too computationally demanding for structures with lots of atoms in the unit cell. In such cases more elaborate schemes are required. In 1985 Leslie and Gillan [94] proposed a correction to the defect formation energy (Eq. 3.35) that corresponds to the energy of an periodic array of point charges in a neutralizing background:

$$E^q_{\text{corr}} = \frac{\alpha q^2}{2\varepsilon L} \tag{5.26}$$

where α is the Madelung constant and ε is the macroscopic dielectric constant. Since then more involved schemes have been suggested, where many of them include the correction in Eq. 5.26 as well as additional electrostatic consideration, such as different model charge distributions and potential alignment [95–101]. The latter is a correction that aligns the potential of the defective and ideal supercell, which are different since the number of ions in the two systems is different. Assessment of some of these schemes has shown that they all work reasonably well for defects with localized charge distributions but not for delocalized defects [101, 102].

Charged point defects have been studied in all papers in this thesis, thus the need for correction schemes has been an important aspect in this work. In Paper I Eq. 5.25 was used to extrapolate formation energies in $BaZrO_3$. This approach is quite suitable for this material since the dielectric constant is large [45] and therefore the energy converges rather quickly with respect to cell size due to screening. The correction is expected to work well since the considered defects have a localized charge distribution. Regarding the work on grain boundaries (Papers II-IV) no corrections were employed. This choice was motivated by the fact the all formation energies were calculated using the same cell size and thus the errors are expected to cancel to large extent in the segregation energies.

The band gap problem of DFT (see Section 5.1.4) also has a severe effect on defect formation energies. The formation energy of charged defects depend on the position of the valence and conduction band edges, which can be quite misplaced. It is also possible that defect levels, which should be located inside the band gap, end up within the valence or conduction band, which can alter the defect properties. A straightforward approach to correct for these errors is simply to use computational methods that treats the band gap more accurately, e.g., hybrid functionals or *GW* calculations. This can however be very computationally demanding, especially for defects associated with large supercell sizes. A different approach which does not require explicit calculations of defects with these demanding methods is to apply a band gap correction directly to Eq. 3.35 [103, 104]. In this way, only one calculation beyond standard DFT is necessary in order to correct the band gap and the band edge shifts. A problem with this method is that it is not always obvious how defect levels behave when the band gap opens up and this information is not

obtained from the ideal system. However, in the special case of fully ionized defects only the shift of the valence band is of importance [105]. In this case is the band gap correction to Eq. 3.35 given by

$$E_{\text{corr}}^{\text{gap}} = q\Delta\varepsilon_{\text{vbm}} \tag{5.27}$$

where $\Delta\varepsilon_{\text{vbm}} = \varepsilon_{\text{vbm}} - \varepsilon_{\text{vbm}}^{\text{DFT}}$ is the valence band shift. This correction was employed in Paper I together with $\Delta\varepsilon_{\text{vbm}}$ calculated from G_0W_0 calculations.

5.2 *GW*-approximation

Although DFT works very well for many systems some properties are not well described such as the band gap, which was discussed in the previous section. The fact that DFT is ground state theory means that it does not describe excitations properly. Thus, methods beyond standard DFT are necessary to model such interactions and related properties. A concept that many such methods revolve around is that of *quasiparticles*. The repulsive character of the electron-electron interaction in solids forms effective positively charged regions around the electrons, which screens the interaction between electrons. Within this context the quasiparticle is defined as the combined entity of the electron and the positive surrounding charge. Quasiparticles interact through a screened Coulomb interaction, W, which is weaker compared to the bare Coulomb interaction between electrons, v.

The mathematical description of quasiparticles is based on the single particle Green's function G. G is referred to as a propagator, which describes the movement of the quasiparticle. G is related to the quasiparticle wave functions Φ_i and energies E_i through the expression

$$G(\mathbf{r}, \mathbf{r}'; E) = \sum_i \frac{\Phi_i(\mathbf{r})\Phi_i^*(\mathbf{r}')}{E - E_i} \tag{5.28}$$

which only depends on six spatial degrees of freedom, and thus G is a more manageable quantity compared to the many-body wave function. The behavior of quasiparticles is governed by the quasiparticle equation

$$\left[-\frac{1}{2}\nabla^2 + V_{\text{H}}(\mathbf{r}) + V_{\text{ext}}(\mathbf{r})\right]\Phi_i(\mathbf{r}) + \int \Sigma(\mathbf{r}, \mathbf{r}'; E_i)\Phi_i(\mathbf{r}')\mathrm{d}\mathbf{r}' = E_i\Phi_i(\mathbf{r}) \tag{5.29}$$

where $V_{\text{H}}(\mathbf{r})$ is the Hartree potential (see Eq. 5.12), $V_{\text{ext}}(\mathbf{r})$ is the external potential and $\Sigma(\mathbf{r}, \mathbf{r}'; E_i)$ is the self-energy, which contains all many-body effects not included in the Hartree approximation. To obtain an exact expression for the self-energy is not possible due to the complex nature of the included many-body effects and

approximations for this quantity are therefore needed. In 1965, Hedin proposed [106] that the self-energy could be expressed as

$$\Sigma = GW \tag{5.30}$$

This approximation is referred to as the *GW*-approximation[2] (GWA). Beside the expression in Eq. 5.30, G and Σ are also related through the Dyson equation

$$G = G_0 + G_0 \Sigma G, \tag{5.31}$$

where G_0 is the non-interacting single particle Green's function. Similar to the expression for G in Eq. 5.28 G_0 is given by

$$G_0(\mathbf{r}, \mathbf{r}'; E) = \sum_i \frac{\psi_i(\mathbf{r})\psi_i^*(\mathbf{r}')}{E - \varepsilon_i} \tag{5.32}$$

where ψ_i and ε_i are the wave functions and energies for non-interacting particles, which can be obtained from e.g. DFT or HF. Additionally, the quasiparticle energies can be expressed in terms of ε_i according to

$$E_i = \varepsilon_i + \langle \psi_i | \Sigma(E_i) - V_{\text{xc}} | \psi_i \rangle \approx \varepsilon_i + Z_i \langle \psi_i | \Sigma(\varepsilon_i) - V_{\text{xc}} | \psi_i \rangle \tag{5.33}$$

where V_{xc} is the xc-potential (Eq. 5.13 for DFT) and the quasiparticle weight $Z_i = \left[1 - \partial \Sigma_i(E)/\partial E|_{E=\varepsilon_i}\right]^{-1}$, with $\Sigma_i(E) \equiv \langle \psi_i | \Sigma(E) | \psi_i \rangle$.

The determination of Σ requires knowledge of G and vice versa, and a solution can therefore only be obtained in an iterative, self-consistent manner. An evaluation of a *GW* self-consistency cycle starts with a Green's function G. Based on this function the polarization P can be determined which is then used to calculate the dielectric function ε. In turn, the screened Coulomb interaction can be determined according to $W = \varepsilon^{-1} v$ and Eq. 5.30 can then be used to determine the self-energy. Finally, a new Green's function G is obtained using Eq. 5.31. In order to perform an actual *GW* calculation an initial guess for G is required. In practice G_0 is used as a starting point which corresponds to $\Sigma = 0$, and the corresponding screened Coulomb interaction is denoted W_0.

There are several different ways to perform *GW* calculations, which differ in the way G and W are updated and this is reflected in their names. G_0W_0 refers to the perturbative approach when neither G or W are updated which corresponds to simply determining the self-energy once and then calculating E_i using Eq. 5.33. This approach has been considered in Paper I. Following the same logic, GW_0 refers to when G is updated while W is kept fixed, and *GW* in this context is when both G and W are updated.

[2]More comprehensive reviews on the subject of *GWA* can be found in [107, 108].

5.3 Interatomic potentials

While DFT is very successful in describing properties of many materials the method suffers from substantial computational cost, which puts a limit on system size on the order of 1000 atoms. Many problems require more atoms in order to obtain a proper description of the specific task at hand. In many such cases interatomic potentials can be used instead. Here the electronic problem is embedded into an interatomic potential, which describes the interaction between atoms or ions, or both. The potential is fitted to experimental or first-principles data in order to model the considered system. The number of particles in the system is reduced considerably with this approximation, since only the nuclei are treated explicitly, which allows for larger system sizes.

In general the potential energy of a system can be written as a sum of interactions of different order

$$V(\mathbf{r}_1, ..., \mathbf{r}_N) = \sum_i U_1(\mathbf{r}_i) + \sum_i \sum_{j>i} U_2(\mathbf{r}_i, \mathbf{r}_j) + \sum_i \sum_{j>i} \sum_{k>j>i} U_3(\mathbf{r}_i, \mathbf{r}_j, \mathbf{r}_k) + \dots \quad (5.34)$$

where U_n corresponds to interactions including n particles. The significance of the different terms in Eq. 5.34 depends on the character of the specific problem. The simplest potentials only include the U_2 term and depend only on the interatomic distance and a few material specific parameters. These are termed *pair-potentials* and are suitable for describing systems where electrons are well localized on atoms and ions, such as systems with ionic and van der Waals bonding. One of the most well known pair potential is the Lennard-Jones potential [109], which is used to describe interactions between noble gas atoms. For systems where electrons are more delocalized these simple pair potentials are no longer sufficient. This is the case for systems with metallic bonding. Here many-body interactions become important and higher order terms in Eq. 5.34 have to be included.

It is not only the bonding character that determines the potential form. Different structures of the same material may require different treatments, such as interfaces and surfaces. Also, in dynamic simulations bonds can be formed and broken and this requires further considerations. The fact that the same potential does not always work for different systems is one of the main drawbacks with this approach, since many problems require input from different sources. The ability of a potential to describe different systems is referred to as the *transferability*. Additionally, a potential of a specific form can be parameterized differently depending on which types of properties or data considered in the fitting procedure, highlighting this problem even more.

In Paper II an interatomic potential was used to model grain boundary structures in $BaZrO_3$. The bonding in this material is of ionic character and was modeled using a Buckingham potential [110] together with Coulomb interactions, which

corresponds to a pair potential of the form

$$U_{ij}(r_{ij}) = A_{ij} \exp\left(-B_{ij} r_{ij}\right) + \frac{C_{ij}}{r_{ij}^6} + \frac{q_i q_j}{r_{ij}} \tag{5.35}$$

where A_{ij}, B_{ij} and C_{ij} are parameters that depend on the species of i and j, q_i and q_j are the ionic charges, and $r_{ij} = \left|\mathbf{r}_i - \mathbf{r}_j\right|$ is the interatomic distance. The Buckingham potential is the first and second term, which describe Pauli repulsion and van der Waals bonding respectively. The shell-model [111] was also considered which is a way to include electronic polarizability, which is lacking within the Buckingham potential. This model separates the ion into a core and a massless shell, which are connected through a harmonic spring. Both core and shell are associated with charges that sum up to the formal charge of the ion. The specific values used for the Buckingham and shell-model parameters in Paper II in order to study $BaZrO_3$ were taken from [112].

6 Summary of the papers

6.1 Paper I: Hydration and oxidation

The purpose of this paper was to study the implications of the band gap problem of DFT on the hydration (Eq. 2.4) and oxidation (Eq. 2.5) of oxygen vacancies in acceptor-doped $BaZrO_3$. These two reactions are decisive for $BaZrO_3$ and other perovskites when used as ionic and electronic conductors. The band gap, or more precisely the position of the valence band edge, directly influence the formation energy of the involved defects (2+ charged oxygen vacancies, protons and holes) and a proper description of the band gap is therefore of great importance. The two reactions have been studied using first-principles methods to calculate defect formation energies in conjunction with thermodynamic modeling in order to obtain equilibrium defect concentrations for various temperatures and partial pressures.

Three different methods have been considered for the calculations of the band gap: PBE, PBE0 and G_0W_0. As expected, PBE underestimates the band gap with about 40% (3.13 eV compared with the experimental results 4.8-5.3 eV). Both PBE0 and G_0W_0 predict a more reasonable band gap, 5.35 eV and 4.73 eV respectively. The shift of the valence band with respect to PBE was determined to be -1.42 eV for PBE0 and -1.10 eV for G_0W_0. Furthermore, these three methods have been used to calculate defect formation energies. While PBE and PBE0 have been used directly to calculate all the contributions in Eq. 3.35, G_0W_0 have been used as a correction to PBE using the valence band shift according to Eq. 5.27, which further on is referred to as PBE+χ[G_0W_0]. The difference between the PBE and PBE0 formation energies was found to be very close to $q\cdot\Delta\varepsilon_{\mathrm{vbm}}$ which confirms the validity of the PBE+χ[G_0W_0] approach.

For the hydration reaction PBE is previously known to yield reasonable results, which was also confirmed here. This reaction is independent of the position

of the valence band edge and therefore is PBE+$\chi[G_0W_0]$ equivalent to PBE in this case. PBE0 gave only slightly different results, still consistent with PBE as well as experimental data. A different picture is obtained for the oxidation reaction since the corresponding enthalpy follows a dependence of $2\varepsilon_{\mathrm{vbm}}$. Thus, the consequence of the valence band shifts is that the oxidation enthalpy is changed by more than 2 eV. More importantly, the enthalpy switches sign which changes the character of the reaction from exothermic with PBE to endothermic with PBE0 and PBE+$\chi[G_0W_0]$. There is no experimental data available for the oxidation enthalpy in $BaZrO_3$ in the literature. There are however reported values for other perovskites ($BaCeO_3$, $BaTiO_3$ and $SrTiO_3$) which all suggest an endothermic reaction.

The qualitative difference between the methods has a huge impact on results from the thermodynamic modeling. The exothermic nature of PBE leads to extremely large hole concentrations which almost completely compensate the charge of the dopant ions under dry conditions except at very low oxygen partial pressures. There is still a substantial amount of holes present during hydrated conditions and they compensate about half of the dopant charge at low temperatures while protons compensate the other half.

With PBE0 and PBE+$\chi[G_0W_0]$ oxygen vacancies becomes the main charge carrier under dry conditions and holes only become dominant at high temperatures and high oxygen partial pressures. Additionally, almost a completely protonated material is obtained under wet conditions and the hole concentration is order of magnitude lower than the proton concentration in this case. This is more in line with results in the literature as almost completely hydrated samples have been obtained experimentally.

Finally, the hole concentrations have been compared with experimental data on the hole conductivity in Y-doped $BaZrO_3$. Such a comparison requires the knowledge of the hole mobility, which for $BaZrO_3$ is unknown. However, by assuming an essentially band-like conduction mechanism PBE0 and PBE+$\chi[G_0W_0]$ yield activation energies similar to those found experimentally. This is not at all the case for PBE and an agreement with the experimental conductivity data is only obtained by assuming a hopping mechanism with very large migration barriers.

6.2 Papers II-IV: Space-charge formation at grain boundaries

There is experimental evidence that space-charges at grain boundaries in acceptor-doped $BaZrO_3$ impede the proton conductivity across these interfaces thus limiting the overall proton conductivity in these materials. The aim of these papers was to study and elucidate the mechanism behind the space-charge formation by the

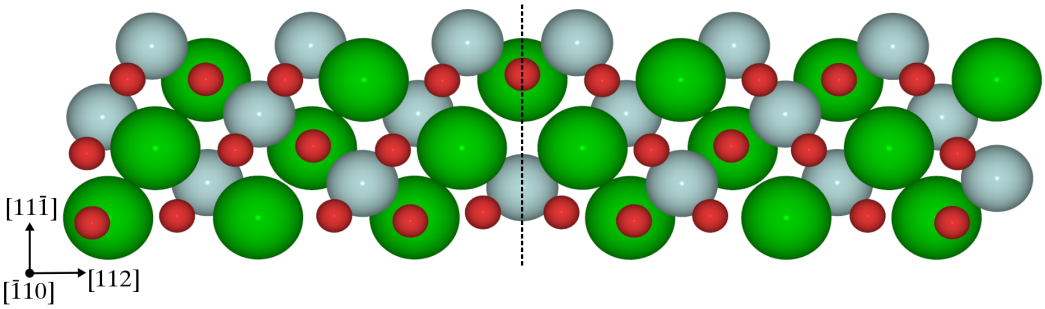

Figure 6.1: The (112)[$\bar{1}$10] tilt grain boundary in $BaZrO_3$. The dashed line indicates the grain boundary interface. The green, grey and red atoms correspond barium, zirconium and oxygen respectively.

means of atomistic modeling. The grain boundaries under consideration are stoichiometric tilt boundaries with symmetric grain orientations. As an example, the (112)[$\bar{1}$10] grain boundary is shown in Fig. 6.1. The notation of the grain boundaries is such that the grain boundary plane, which corresponds to the direction perpendicular to the boundary interface, is given in parentheses while the tilt axis, which is parallel to the interface, is given in square brackets. The same methodology was employed in all three papers with segregation energies calculated using Eq. 3.43 and space-charge modeling according to the theory in Section 3.6. The main difference between the papers is that an interatomic potential was used in Paper II while DFT was used in Papers III and IV. Additionally, oxygen vacancy segregation was treated in all papers while proton segregation was only considered in the latter two.

The reason for using an interatomic potential in Paper II was to be able to model larger grain boundary structures not accessible with DFT. Eight different boundaries were considered, all with tilt axis [$\bar{1}$10] and with the boundary planes $(111), (112), \ldots, (118)$. The smallest two boundaries, (111) and (112), have previously been studied using DFT and the results compare well concerning both grain boundary structures and energies as well as segregation energies. Oxygen vacancy segregation was found to be favorable in all grain boundaries with segregation energies within the range -0.5 eV to -2.0 eV. The majority of all non-zero segregation energies were found within 5 Å of the boundary interfaces which corresponds to a core region of 10 Å. Space-charge modeling based on these segregation energies yield space-charge potentials between 0.2 V and 0.8 V at a temperature of 600 K, which are comparable to experimental data. Two different dopant concentrations were considered (5% and 10%) which both gave very similar results.

The considered grain boundaries in Paper III were (111)[$\bar{1}$10], (112)[$\bar{1}$10] and (210)[001] with mirror-symmetric atomic structures. The latter was also considered in Paper IV but the atomic structure was further optimized using rigid body translations, which resulted in a non-symmetric configuration. Both oxygen vacancies and protons were found to segregate to all grain boundaries and the same sites were in general preferred by both defects. The most favorable vacancy segregation energies were found to be in the range −0.5 eV to −1.5 eV while the same range was −0.7 eV to −1.3 eV for the protons. No direct trend was observed for the segregation strength as some boundaries favored proton segregation while others favored vacancy segregation.

Applying the space-charge model to these results gave for dry conditions (i.e. only consider oxygen vacancies) similar results compared to Paper II with potential barriers between 0.2 V and 0.7 V, which are directly related to the strength of the segregation energies. However, this behavior is changed when protons were taken into consideration. The space-charge potentials under wet conditions are all very similar and lie in the interval between 0.6 V and 0.7 V at temperatures below 800 K. Thus, some potential barriers change quite a lot between dry and wet conditions while others remain unchanged. Both scenarios have been seen experimentally although the difference in the observed potential change was smaller. Furthermore, concentration profiles shows that all grain boundaries become hydrated at low temperatures despite the fact that different boundaries favors different defects, which explains why the potential barriers become so similar. What differs is the hydration temperature, which increases for boundaries where proton segregation is preferred.

To conclude, both oxygen vacancies and protons are found to segregate to a large set of grain boundaries in $BaZrO_3$ and give rise to space-charge formation. Potential barriers are in agreement with experimental data, which gives an indication that the low grain boundary proton conductivity can be explained in terms of space-charge formation. Additionally, protons seem to be the prime source to space-charge formation in wet atmospheres for temperatures below 800 K, which are typical conditions for fuel cell applications.

7

Outlook

The research done in the first part of this thesis show how important the prediction of the band gap is for oxidation and hole formation in acceptor-doped barium zirconate and related materials. While it is possible to make assumptions that justify an exothermic oxidation reaction to some extent, the results shown here with an endothermic reaction give a much more satisfactory agreement with experimental data, both concerning defect concentrations as well as conductivity. Despite the current improvement, there are still aspects regarding oxidation and holes that are still not clear, which could be subject to further investigation. One such aspect is the physical nature of the hole which here is treated as a delocalized band state. DFT studies on similar systems ($BaTiO_3$, $SrTiO_3$ and $CaTiO_3$) based on the HSE functional and the DFT+U method have shown that the hole interact with the lattice and forms a small polaron [113, 114]. It is possible that this is the case in $BaZrO_3$ as well, and if so, this would affect the oxidation enthalpy and consequently the hole concentration.

The effect of the dopant ions is also an important aspect that could further addressed. While the qualitative effect the dopant is quite clear the implicit treatment considered here leaves much to be desired when it comes to a quantitative agreement with experimental data as these results varies for different dopant species and concentrations. With the thermodynamic scheme presented here these effects can be included in a straightforward manner by explicitly considering defect-dopant association.

It could also be of interest to study the band gap in more detail. Even though the band gap is significantly improved with PBE0 and G_0W_0 there is still a difference between the two methods and it is not clear which one of them that is most accurate. The VBM difference of about 0.3 eV changes the hole concentration with one or more orders of magnitude (see Fig. 7 in Paper I). Beside further the-

oretical investigations, this would require more input from experiments, as there is some scatter in the band gap results in the literature. More experimental data is also necessary for a quantitative comparison of the oxidation enthalpy and hole mobility, where the latter can be obtained with e.g., Hall measurements.

The mechanism behind space-charge formation was clarified in the second part of the thesis. Defect segregation is the driving force and protons seem to play the biggest part under hydrated conditions. While a qualitative understanding of the phenomenon has been obtained, there are still aspects to consider.

Similar to the oxidation, the treatment of the dopants is simplified in the current approach and can be further improved. There are multiple aspects to consider here. First, the dopants are only considered implicitly through the space-charge modeling and only the concentration have an impact, not the species. In reality, it is most probable that the segregation energies are affected by defect-dopant interactions, which (at least in the bulk phase [115, 116]) varies for different dopant species.

Second, the dopants are uniformly distributed throughout the material in the present model but this is not necessarily the case. Different synthesis routes can yield different microstructures [51] and dopant segregation to grain boundaries have been observed in yttrium- and scandium-doped samples [31, 44, 47, 117]. If dopant were to be mobile then they would segregate to the boundary due to the attractive space-charge potential. There is also a possibility that the segregation could be driven by favorable segregation energies. An increased dopants concentration at the grain boundaries will in turn attract more positive defects.

Finally, for high defect concentrations defect-defect interactions become important as this could alter the segregation energies. This would require a more elaborate space-charge model that can take these interactions into account.

Acknowledgments

First of all I would like to express my sincerest gratitude towards my main supervisor *Göran Wahnström* for his guidance and support throughout the first part of my ongoing Ph.D. project. My assistant supervisor *Paul Erhart* also deserves a great deal of appreciation. He always finds time to answer my questions and he has been invaluable for my understanding of the work related to the first paper in this thesis. I am also greatly indebted to *Edit Helgee* and *Joakim Nyman* for helping me getting started when I joined the MST group as a master student as well as for putting a huge effort into the work on the grain boundary project. Finally, I thank all present and former members of the MST group for contributing to a pleasant and stimulating working environment.

Working and studying at Chalmers is not always a walk in the park and therefore I would especially like to thank two of my former classmates, *Emil* and *Nils*, which have been my fellow companions during my years at Chalmers. They have given me lots of fond memories from quiz nights and late nights on the pub. My friends from outside Chalmers also deserve credit for distracting me from work on a regular basis. See you on Saturday!

I would also like to thank my parents *Solvig* and *Mats* for all their support, especially during the time when this thesis was written. Last, but certainly not the least, I would like to thank *Magdalena* and *Frank* for making our home a fun and happy place. Life would be quite boring without you.

Bibliography

[1] G. W. Crabtree, M. S. Dresselhaus, and M. V. Buchanan, *The hydrogen economy*, Physics Today **57**, 39 (2004).

[2] L. Carrette, K. A. Friedrich, and U. Stimming, *Fuel Cells – Fundamentals and Applications*, Fuel Cells **1**, 5 (2001).

[3] B. C. H. Steele and A. Heinzel, *Materials for fuel-cell technologies*, Nature **414**, 345 (2001).

[4] A. Kirubakaran, S. Jain, and R. K. Nema, *A review on fuel cell technologies and power electronic interface*, Renewable and Sustainable Energy Reviews **13**, 2430 (2009).

[5] E. Helgee, Licentiate thesis, Chalmers University of Technology, 2013.

[6] E. Fabbri, L. Bi, D. Pergolesi, and E. Traversa, *Towards the Next Generation of Solid Oxide Fuel Cells Operating Below 600 °C with Chemically Stable Proton-Conducting Electrolytes*, Advanced Materials **24**, 195 (2011).

[7] A. J. Jacobson, *Materials for Solid Oxide Fuel Cells*, Chemistry of Materials **22**, 660 (2009).

[8] L. Malavasi, C. A. J. Fisher, and M. S. Islam, *Oxide-ion and proton conducting electrolyte materials for clean energy applications: structural and mechanistic features*, Chemical Society Reviews **39**, 4370 (2010).

[9] H. Iwahara, T. Esaka, H. Uchida, and N. Maeda, *Proton conduction in sintered oxides and its application to steam electrolysis for hydrogen production*, Solid State Ionics **3–4**, 359 (1981).

[10] K. D. Kreuer, *Proton-conducting Oxides*, Annual Review of Materials Research **33**, 333 (2003).

[11] T. Norby, in *Perovskite Oxide for Solid Oxide Fuel Cells*, *Fuel Cells and Hydrogen Energy*, edited by T. Ishihara (Springer US, Boston, Massachusetts, 2009), pp. 217–241.

[12] C. Sun and U. Stimming, *Recent anode advances in solid oxide fuel cells*, Journal of Power Sources **171**, 247 (2007).

[13] D. J. L. Brett, A. Atkinson, N. P. Brandon, and S. J. Skinner, *Intermediate temperature solid oxide fuel cells*, Chemical Society Reviews **37**, 1568 (2008).

[14] A. Orera and P. R. Slater, *New Chemical Systems for Solid Oxide Fuel Cells*, Chemistry of Materials **22**, 675 (2009).

[15] J. W. Fergus, *Metallic interconnects for solid oxide fuel cells*, Materials Science and Engineering: A **397**, 271 (2005).

[16] P. C. K. Vesborg and T. F. Jaramillo, *Addressing the terawatt challenge: scalability in the supply of chemical elements for renewable energy*, RSC Advances **2**, 7933 (2012).

[17] M. E. Lines and A. M. Glass, *Principles and Applications of Ferroelectrics and Related Materials* (Oxford University Press, New York, 1977).

[18] K. M. Rabe, C. H. Ahn, and J.-M. Triscone, *Physics of Ferroelectrics: A Modern Perspective* (Springer Science & Business Media, Berlin Heidelberg, 2007).

[19] V. V. Kharton, F. M. B. Marques, and A. Atkinson, *Transport properties of solid oxide electrolyte ceramics: a brief review*, Solid State Ionics **174**, 135 (2004).

[20] J. Sunarso, S. Baumann, J. M. Serra, W. A. Meulenberg, S. Liu, Y. S. Lin, and J. C. Diniz da Costa, *Mixed ionic–electronic conducting (MIEC) ceramic-based membranes for oxygen separation*, Journal of Membrane Science **320**, 13 (2008).

[21] C. S. Koonce, M. L. Cohen, J. F. Schooley, W. R. Hosler, and E. R. Pfeiffer, *Superconducting Transition Temperatures of Semiconducting $SrTiO_3$*, Physical Review **163**, 380 (1967).

[22] T. D. Thanh, A. Koma, and S. Tanaka, *Superconductivity in the $BaPb_{1-x}$ Bi_x O_3 system*, Applied physics **22**, 205 (1980).

[23] R. J. Cava, B. Batlogg, R. B. van Dover, D. W. Murphy, S. Sunshine, T. Siegrist, J. P. Remeika, E. A. Rietman, S. Zahurak, and G. P. Espinosa, *Bulk superconductivity at 91 K in single-phase oxygen-deficient perovskite $Ba_2YCu_3O_{9-\delta}$*, Physical Review Letters **58**, 1676 (1987).

[24] G. H. Jonker and J. H. Van Santen, *Ferromagnetic compounds of manganese with perovskite structure*, Physica **16**, 337 (1950).

[25] R. M. Kusters, J. Singleton, D. A. Keen, R. McGreevy, and W. Hayes, *Magnetoresistance measurements on the magnetic semiconductor* $Nd_{0.5}Pb_{0.5}MnO_3$, Physica B: Condensed Matter **155**, 362 (1989).

[26] R. von Helmolt, J. Wecker, B. Holzapfel, L. Schultz, and K. Samwer, *Giant negative magnetoresistance in perovskitelike* $La_{2/3}Ba_{1/3}MnO_x$ *ferromagnetic films*, Physical Review Letters **71**, 2331 (1993).

[27] H. Iwahara, Y. Asakura, K. Katahira, and M. Tanaka, *Prospect of hydrogen technology using proton-conducting ceramics*, Solid State Ionics **168**, 299 (2004).

[28] J. W. Phair and S. P. S. Badwal, *Review of proton conductors for hydrogen separation*, Ionics **12**, 103 (2006).

[29] O. Auciello, J. F. Scott, and R. Ramesh, *The Physics of Ferroelectric Memories*, Physics Today **51**, 22 (1998).

[30] M. A. Peña and J. L. G. Fierro, *Chemical Structures and Performance of Perovskite Oxides*, Chemical Reviews **101**, 1981 (2001).

[31] F. Iguchi, N. Sata, and H. Yugami, *Proton transport properties at the grain boundary of barium zirconate based proton conductors for intermediate temperature operating SOFC*, Journal of Materials Chemistry **20**, 6265 (2010).

[32] A. M. Glazer, *The classification of tilted octahedra in perovskites*, Acta Crystallographica Section B Structural Crystallography and Crystal Chemistry **28**, 3384 (1972).

[33] T. Pagnier, I. Charrier-Cougoulic, C. Ritter, and G. Lucazeau, *A neutron diffraction study of* $BaCe_x\ Zr_{1-x}O_3$, The European Physical Journal - Applied Physics **9**, 1 (2000).

[34] I. Levin, T. G. Amos, S. M. Bell, L. Farber, T. A. Vanderah, R. S. Roth, and B. H. Toby, *Phase equilibria, crystal structures, and dielectric anomaly in the* $BaZrO_3$–$CaZrO_3$ *system*, Journal of Solid State Chemistry **175**, 170 (2003).

[35] H. G. Bohn and T. Schober, *Electrical Conductivity of the High-Temperature Proton Conductor* $BaZr_{0.9}Y_{0.1}O_{2.95}$, Journal of the American Ceramic Society **83**, 768 (2000).

[36] F. Iguchi, T. Yamada, N. Sata, T. Tsurui, and H. Yugami, *The influence of grain structures on the electrical conductivity of a $BaZr_{0.95}Y_{0.05}O_3$ proton conductor*, Solid State Ionics **177**, 2381 (2006).

[37] P. Babilo, T. Uda, and S. M. Haile, *Processing of yttrium-doped barium zirconate for high proton conductivity*, Journal of Materials Research **22**, 1322 (2007).

[38] M. Shirpour, R. Merkle, C. T. Lin, and J. Maier, *Nonlinear electrical grain boundary properties in proton conducting Y–$BaZrO_3$ supporting the space charge depletion model*, Physical Chemistry Chemical Physics **14**, 730 (2011).

[39] F. Iguchi, T. Tsurui, N. Sata, Y. Nagao, and H. Yugami, *The relationship between chemical composition distributions and specific grain boundary conductivity in Y-doped $BaZrO_3$ proton conductors*, Solid State Ionics **180**, 563 (2009).

[40] P. I. Dahl, H. L. Lein, Y. Yu, J. Tolchard, T. Grande, M.-A. Einarsrud, C. Kjølseth, T. Norby, and R. Haugsrud, *Microstructural characterization and electrical properties of spray pyrolyzed conventionally sintered or hot-pressed $BaZrO_3$ and $BaZr_{0.9}Y_{0.1}O_{3-\delta}$*, Solid State Ionics **182**, 32 (2011).

[41] M. Shirpour, R. Merkle, and J. Maier, *Space charge depletion in grain boundaries of $BaZrO_3$ proton conductors*, Solid State Ionics **225**, 304 (2012).

[42] D.-H. Kim, B.-K. Kim, and Y.-C. Kim, *Energy barriers for proton migration in yttrium-doped barium zirconate super cell with Σ5 (310)/[001] tilt grain boundary*, Solid State Ionics **213**, 18 (2012).

[43] J.-H. Yang, D.-H. Kim, B.-K. Kim, and Y.-C. Kim, *High activation energy for proton migration at tilt grain boundary in barium zirconate*, Solid State Ionics **252**, 126 (2013).

[44] C. Kjølseth, H. Fjeld, Ø. Prytz, Ø. Prytz, P. I. Dahl, C. Estournès, R. Haugsrud, and T. Norby, *Space-charge theory applied to the grain boundary impedance of proton conducting $BaZr_{0.9}Y_{0.1}O_{3-\delta}$*, Solid State Ionics **181**, 268 (2010).

[45] C.-T. Chen, C. E. Danel, and S. Kim, *On the origin of the blocking effect of grain-boundaries on proton transport in yttrium-doped barium zirconates*, Journal of Materials Chemistry **21**, 5435 (2011).

[46] F. Iguchi, C.-T. Chen, H. Yugami, and S. Kim, *Direct evidence of potential barriers at grain boundaries in Y-doped $BaZrO_3$ from dc-bias dependence measurements*, J. Mater. Chem. **21**, 16517 (2011).

[47] M. Shirpour, B. Rahmati, W. Sigle, P. A. van Aken, R. Merkle, and J. Maier, *Dopant Segregation and Space Charge Effects in Proton-Conducting $BaZrO_3$ Perovskites*, J. Phys. Chem. C **116**, 2453 (2012).

[48] M. Shirpour, R. Merkle, and J. Maier, *Evidence for space charge effects in Y-doped $BaZrO_3$ from reduction experiments*, Solid State Ionics **216**, 1 (2012).

[49] J. B. Nyman, E. E. Helgee, and G. Wahnström, *Oxygen vacancy segregation and space-charge effects in grain boundaries of dry and hydrated $BaZrO_3$*, Applied Physics Letters **100**, 061903 (2012).

[50] J. M. Polfus, K. Toyoura, F. Oba, I. Tanaka, and R. Haugsrud, *Defect chemistry of a $BaZrO_3$ Σ3 (111) grain boundary by first principles calculations and space–charge theory*, Physical Chemistry Chemical Physics **14**, 12339 (2012).

[51] S. Ricote, N. Bonanos, A. Manerbino, N. P. Sullivan, and W. G. Coors, *Effects of the fabrication process on the grain-boundary resistance in $BaZr_{0.9}Y_{0.1}O_{3-\delta}$*, Journal of Materials Chemistry A **2**, 16107 (2014).

[52] R. A. De Souza, *The formation of equilibrium space-charge zones at grain boundaries in the perovskite oxide $SrTiO_3$*, Physical Chemistry Chemical Physics **11**, 9939 (2009).

[53] C.-T. Chen, S. K. Kim, M. Ibbotson, A. Yeung, and S. Kim, *Thermionic emission of protons across a grain boundary in 5 mol% Y-doped $SrZrO_3$, a hydrogen pump*, International Journal of Hydrogen Energy **37**, 12432 (2012).

[54] H. J. Park and S. Kim, *Space Charge Effects on the Interfacial Conduction in Sr-Doped Lanthanum Gallates: A Quantitative Analysis*, The Journal of Physical Chemistry C **111**, 14903 (2007).

[55] H. J. Park and S. Kim, *The enhanced electronic transference number at the grain boundaries in Sr-doped $LaGaO_3$*, Solid State Ionics **179**, 1329 (2008).

[56] X. Guo and R. Waser, *Electrical properties of the grain boundaries of oxygen ion conductors: Acceptor-doped zirconia and ceria*, Progress in Materials Science **51**, 151 (2006).

[57] F. A. Kröger and H. J. Vink, in *Solid State Physics*, edited by F. Seitz and D. Turnbull (Academic Press, New York, 1956), Vol. 3, pp. 307–435.

[58] C. Kittel, *Introduction to Solid State Physics*, 8th ed. (John Wiley & Sons, Hoboken, New Jersey, 2005).

[59] C. Freysoldt, B. Grabowski, T. Hickel, J. Neugebauer, G. Kresse, A. Janotti, and C. G. Van de Walle, *First-principles calculations for point defects in solids*, Reviews of Modern Physics **86**, 253 (2014).

[60] J. Maier, *Physical Chemistry of Ionic Materials: Ions and Electrons in Solids* (John Wiley & Sons, Chichester, West Sussex, 2004).

[61] R. A. De Souza, Z. A. Munir, S. Kim, and M. Martin, *Defect chemistry of grain boundaries in proton-conducting solid oxides*, Solid State Ionics **196**, 1 (2011).

[62] Y. Yamazaki, F. Blanc, Y. Okuyama, L. Buannic, J. C. Lucio-Vega, C. P. Grey, and S. M. Haile, *Proton trapping in yttrium-doped barium zirconate*, Nature Materials **12**, 647 (2013).

[63] D. M. Smyth, *The Defect Chemistry of Metal Oxides* (Oxford University Press, New York, 2000).

[64] A. Einstein, *Über die von der molekularkinetischen Theorie der Wärme geforderte Bewegung von in ruhenden Flüssigkeiten suspendierten Teilchen*, Annalen der Physik **322**, 549 (1905).

[65] K. D. Kreuer, *Proton Conductivity: Materials and Applications*, Chemistry of Materials **8**, 610 (1996).

[66] K. D. Kreuer, *Aspects of the formation and mobility of protonic charge carriers and the stability of perovskite-type oxides*, Solid State Ionics **125**, 285 (1999).

[67] M. Born and R. Oppenheimer, *Zur Quantentheorie der Molekeln*, Annalen der Physik **389**, 457 (1927).

[68] R. Feynman, *Forces in Molecules*, Physical Review **56**, 340 (1939).

[69] W. Kohn, *Nobel Lecture: Electronic structure of matter—wave functions and density functionals*, Reviews of Modern Physics **71**, 1253 (1999).

[70] R. M. Martin, *Electronic Structure: Basic Theory and Practical Methods* (Cambridge University Press, Cambridge, 2004).

[71] J. Kohanoff, *Electronic Structure Calculations for Solids and Molecules: Theory and Computational Methods* (Cambridge University Press, Cambridge, 2006).

[72] K. Capelle, *A bird's-eye view of density-functional theory*, Brazilian Journal of Physics **36**, 1318 (2006).

[73] P. Hohenberg and W. Kohn, *Inhomogeneous Electron Gas*, Physical Review **136**, B864 (1964).

[74] W. Kohn and L. J. Sham, *Self-Consistent Equations Including Exchange and Correlation Effects*, Physical Review **140**, A1133 (1965).

[75] J. P. Perdew, K. Burke, and M. Ernzerhof, *Generalized Gradient Approximation Made Simple*, Physical Review Letters **77**, 3865 (1996).

[76] J. P. Perdew, R. G. Parr, M. Levy, and J. L. Balduz, *Density-Functional Theory for Fractional Particle Number: Derivative Discontinuities of the Energy*, Physical Review Letters **49**, 1691 (1982).

[77] J. P. Perdew and M. Levy, *Physical Content of the Exact Kohn-Sham Orbital Energies: Band Gaps and Derivative Discontinuities*, Physical Review Letters **51**, 1884 (1983).

[78] L. J. Sham and M. Schlüter, *Density-Functional Theory of the Energy Gap*, Physical Review Letters **51**, 1888 (1983).

[79] R. W. Godby, M. Schlüter, and L. J. Sham, *Accurate Exchange-Correlation Potential for Silicon and Its Discontinuity on Addition of an Electron*, Physical Review Letters **56**, 2415 (1986).

[80] P. Mori-Sánchez, A. J. Cohen, and W. Yang, *Localization and Delocalization Errors in Density Functional Theory and Implications for Band-Gap Prediction*, Physical Review Letters **100**, 146401 (2008).

[81] A. D. Becke, *A new mixing of Hartree–Fock and local density-functional theories*, The Journal of Chemical Physics **98**, 1372 (1993).

[82] A. D. Becke, *Density-functional thermochemistry. III. The role of exact exchange*, The Journal of Chemical Physics **98**, 5648 (1993).

[83] A. D. Becke, *Density-functional thermochemistry. IV. A new dynamical correlation functional and implications for exact-exchange mixing*, The Journal of Chemical Physics **104**, 1040 (1996).

[84] V. Fock, *Näherungsmethode zur Lösung des quantenmechanischen Mehrkörperproblems*, Zeitschrift für Physik **61**, 126 (1930).

[85] J. P. Perdew, M. Ernzerhof, and K. Burke, *Rationale for mixing exact exchange with density functional approximations*, The Journal of Chemical Physics **105**, 9982 (1996).

[86] J. Heyd, G. E. Scuseria, and M. Ernzerhof, *Hybrid functionals based on a screened Coulomb potential*, The Journal of Chemical Physics **118**, 8207 (2003).

[87] J. Heyd, G. E. Scuseria, and M. Ernzerhof, *Erratum: "Hybrid functionals based on a screened Coulomb potential" [J. Chem. Phys.118, 8207 (2003)]*, The Journal of Chemical Physics **124**, 219906 (2006).

[88] F. Bloch, *Über die Quantenmechanik der Elektronen in Kristallgittern*, Zeitschrift für Physik **52**, 555 (1929).

[89] D. R. Hamann, M. Schlüter, and C. Chiang, *Norm-Conserving Pseudopotentials*, Physical Review Letters **43**, 1494 (1979).

[90] D. Vanderbilt, *Soft self-consistent pseudopotentials in a generalized eigenvalue formalism*, Physical Review B **41**, 7892 (1990).

[91] P. E. Blöchl, *Projector augmented-wave method*, Physical Review B **50**, 17953 (1994).

[92] C. W. M. Castleton and S. Mirbt, *Finite-size scaling as a cure for supercell approximation errors in calculations of neutral native defects in InP*, Physical Review B **70**, 195202 (2004).

[93] C. W. M. Castleton, A. Höglund, and S. Mirbt, *Managing the supercell approximation for charged defects in semiconductors: Finite-size scaling, charge correction factors, the band-gap problem, and the ab initio dielectric constant*, Physical Review B **73**, 035215 (2006).

[94] M. Leslie and N. J. Gillan, *The energy and elastic dipole tensor of defects in ionic crystals calculated by the supercell method*, Journal of Physics C: Solid State Physics **18**, 973 (1985).

[95] G. Makov and M. C. Payne, *Periodic boundary conditions in ab initio calculations*, Physical Review B **51**, 4014 (1995).

[96] P. A. Schultz, *Charged Local Defects in Extended Systems*, Physical Review Letters **84**, 1942 (2000).

[97] S. Lany and A. Zunger, *Assessment of correction methods for the band-gap problem and for finite-size effects in supercell defect calculations: Case studies for ZnO and GaAs*, Physical Review B **78**, 235104 (2008).

[98] I. Dabo, B. Kozinsky, N. E. Singh-Miller, and N. Marzari, *Electrostatics in periodic boundary conditions and real-space corrections*, Physical Review B **77**, 115139 (2008).

[99] C. Freysoldt, J. Neugebauer, and C. G. Van de Walle, *Fully \textit{Ab Initio} Finite-Size Corrections for Charged-Defect Supercell Calculations*, Physical Review Letters **102**, 016402 (2009).

[100] S. E. Taylor and F. Bruneval, *Understanding and correcting the spurious interactions in charged supercells*, Physical Review B **84**, 075155 (2011).

[101] Y. Kumagai and F. Oba, *Electrostatics-based finite-size corrections for first-principles point defect calculations*, Physical Review B **89**, 195205 (2014).

[102] H.-P. Komsa, T. T. Rantala, and A. Pasquarello, *Finite-size supercell correction schemes for charged defect calculations*, Physical Review B **86**, 045112 (2012).

[103] C. Persson, Y.-J. Zhao, S. Lany, and A. Zunger, *n-type doping of $CuInSe_2$ and $CuGaSe_2$*, Physical Review B **72**, 035211 (2005).

[104] D. Åberg, P. Erhart, A. J. Williamson, and V. Lordi, *Intrinsic point defects in aluminum antimonide*, Physical Review B **77**, 165206 (2008).

[105] H. Peng, D. O. Scanlon, V. Stevanovic, J. Vidal, G. W. Watson, and S. Lany, *Convergence of density and hybrid functional defect calculations for compound semiconductors*, Physical Review B **88**, 115201 (2013).

[106] L. Hedin, *New Method for Calculating the One-Particle Green's Function with Application to the Electron-Gas Problem*, Physical Review **139**, A796 (1965).

[107] L. Hedin and S. Lundqvist, in *Solid State Physics*, edited by F. Seitz, D. Turnbull, and H. Ehrenreich (Academic Press, New York, New York, 1970), Vol. Volume 23, pp. 1–181.

[108] W. G. Aulbur, L. Jönsson, and J. W. Wilkins, in *Solid State Physics*, edited by H. Ehrenreich and F. Spaepen (Academic Press, San Diego, California, 1999), Vol. Volume 54, pp. 1–218.

[109] J. E. Jones, *On the Determination of Molecular Fields. II. From the Equation of State of a Gas*, Proceedings of the Royal Society of London A: Mathematical, Physical and Engineering Sciences **106**, 463 (1924).

[110] R. A. Buckingham, *The Classical Equation of State of Gaseous Helium, Neon and Argon*, Proceedings of the Royal Society of London. Series A, Mathematical and Physical Sciences **168**, 264 (1938).

[111] B. G. Dick and A. W. Overhauser, *Theory of the Dielectric Constants of Alkali Halide Crystals*, Physical Review **112**, 90 (1958).

[112] S. J. Stokes and M. S. Islam, *Defect chemistry and proton-dopant association in $BaZrO_3$ and $BaPrO_3$*, Journal of Materials Chemistry **20**, 6258 (2010).

[113] P. Erhart, A. Klein, D. Åberg, and B. Sadigh, *Efficacy of the DFT + U formalism for modeling hole polarons in perovskite oxides*, Physical Review B **90**, 035204 (2014).

[114] H. Chen and N. Umezawa, *Hole localization, migration, and the formation of peroxide anion in perovskite $SrTiO_3$*, Physical Review B **90**, 035202 (2014).

[115] P. G. Sundell, M. E. Björketun, and G. Wahnström, *Thermodynamics of doping and vacancy formation in $BaZrO_3$ perovskite oxide from density functional calculations*, Physical Review B **73**, 104112 (2006).

[116] M. E. Björketun, P. G. Sundell, and G. Wahnström, *Structure and thermodynamic stability of hydrogen interstitials in $BaZrO_3$ perovskite oxide from density functional calculations*, Faraday Discussions **134**, 247 (2007).

[117] M. Shirpour, G. Gregori, L. Houben, R. Merkle, and J. Maier, *High spatially resolved cation concentration profile at the grain boundaries of Sc-doped $BaZrO_3$*, Solid State Ionics **262**, 860 (2014).

Paper I

Implications of the band gap problem on oxidation and hydration in acceptor-doped barium zirconate

Anders Lindman, Paul Erhart and Göran Wahnström

(In preparation)

Paper II

Oxygen vacancy segregation in grain boundaries of $BaZrO_3$ using interatomic potentials

Anders Lindman, Edit E. Helgee, B. Joakim Nyman and Göran Wahnström

Solid State Ionics **230**, 27-31 (2013)

Paper III

Origin of space charge in grain boundaries of proton-conducting $BaZrO_3$
Edit E. Helgee, Anders Lindman and Göran Wahnström
Fuel Cells **13**, 19-28 (2013)

Paper IV

Theoretical modeling of defect segregation and space-charge formation in the $BaZrO_3$ (210)[001] tilt grain boundary

Anders Lindman, Edit E. Helgee and Göran Wahnström

Solid State Ionics **252**, 121-125 (2013)